DESIGN AND FABRICATION OF NITRIDE-BASED SOLAR CELLS AND INTEGRATION FOR TANDEM CELL

Taha Ayari

DESIGN AND FABRICATION OF NITRIDE-BASED SOLAR CELLS AND INTEGRATION FOR TANDEM CELL

A Dissertation
Presented to
The Academic Faculty

by

Taha Ayari

In Partial Fulfillment
of the Requirements for the Degree
PhD in the
The School of Electrical and Computer Engineering

Georgia Institute of Technology
August 2018

DESIGN AND FABRICATION OF NITRIDE-BASED SOLAR CELLS AND INTEGRATION FOR TANDEM CELL

Approved by:

Dr. Abdallah Ougazzaden, Advisor
School of Electrical and Computer Engineering
Georgia Institute of Technology

Dr. Ali Adibi
School of Electrical and Computer Engineering
Georgia Institute of Technology

Dr. Jean Paul Salvestrini
School of Electrical and Computer Engineering
Georgia Institute of Technology

Dr. Thomas Sanders
Regents Professor, MSE
Georgia Institute of Technology

Dr. Paul Voss
School of Electrical and Computer Engineering
Georgia Institute of Technology

Date Approved: July 2, 2018

ACKNOWLEDGEMENTS

I would like to express my gratitude to my advisor Dr. Abdallah Ougazzaden. This thesis would not have been possible without his knowledge, expertise, and guidance. Furthermore I feel that his confidence in my work allowed me to grow as a scientist, engineer, and researcher. A heartfelt thanks goes out to the other members of my PhD committee: Dr Jean Paul Salvestrini, Dr. Paul Voss, Dr. Ali Adibi and Dr. Thomas Sanders. The patience and the support of Dr. Jean Paul Salvestrini and Dr. Paul Voss has been unwavering during the completion of this thesis. I would also like to thank the institutions and funding partners that made this work possible. Georgia Tech Lorraine has been very supportive during the completion of my PhD. Generous grants from the French National Research Agency (ANR) under the GANEX Laboratory of Excellence (Grant number ANR-11-LABX-0014) have helped make this work possible. Much of the work has been carried out using the equipment, personnel, and resources of the Georgia Tech-CNRS, UMI2958.

I would like to extend my gratitude personally to the other PhD students and colleagues who have assisted in various ways in the making of this thesis. To Suresh Sundaram, Xin Li, Saiful Alam and Adama Mballo who assisted with MOVPE growth. To Matthew Jordan and Chris Bishop who assisted in micro-fabrication. To Youssef El Gmili and Yacine Halfaya who have assisted with characterization. To Walid Elhuni who helped with the simulation of InGaN solar cells.

Finally and most importantly, I would like to thank my mom, dad and siblings for being with me at every stage of my life. They always taught me the importance of quality

education and have made many sacrifices so I could lead a better life and could get a better education. My dad has always been a source of inspiration to me. It is from him where I learnt the importance of being able to apply my knowledge in the real world. He is one of the smartest persons I have seen in my life and he is the main reason why I kept pushing myself so I could reach his level of technical competence one day. My mom is one of the most patient and disciplined persons I have known in my life. She has always been the central support for our family pushing us to aim high and provided us unconditional support for all the endeavors we undertake. But for their support and sacrifices, I would not have made it to this stage of my life and I could not be more thankful for having such an amazing family.

TABLE OF CONTENTS

LIST OF TABLES

LIST OF FIGURES

SUMMARY

The integration of hybrid opto-electronics consists of assembling several devices, fabricated separately using different and potentially non-compatible processes, onto one common platform to achieve a functional heterogeneous system. This concept can be applied for cost-effective and high performance III-Nitride (III-N) based solar cell applications. InGaN alloys exhibit many favorable photovoltaic properties such as broadband absorption with a tunable bandgap (0.7 eV - 3.4 eV), superior radiation resistance, large absorption coefficients and high saturation velocities. Theoretically, efficiency greater than 40% can be achieved by a multi-junction solar cell composed of four InGaN sub-cells with different In content. However, so far the large lattice mismatch between InN and GaN makes it experimentally difficult to grow good-quality, high In-composition InGaN films and currently impedes the realization of an all InGaN multi-junction solar cell. Thus, a practical use of III-N solar cells could be their combination with mature Si and GaAs based solar cell technologies. In this thesis, we have made significant progress toward developing these hybrid devices by developing a transfer method for InGaN solar cells. We demonstrate wafer-scale Van der Waal epitaxy and fabrication of InGaN-based solar cells on 2D h-BN, the mechanical release of the devices, thanks to the Van der Waal bonded layered h-BN, and their transfer on glass on dielectric mirror as back-side reflector with device results and enhanced performance. The dielectric mirror transmits wavelength above 500 nm allowing the operation of InGaN/Si tandem solar cell for example.

Chapter 1 is an introductory chapter. It introduces the motivation behind this thesis work. The global situation of the photovoltaic market dominated by Si technology and the need for multijunction and tandem technology to exceed 40 % efficiency are highlighted with an emphasis on InGaN-based solar cells.

In chapter 2, we present the basic properties of III-nitride alloys as well as the techniques and equipment used for the growth and materials characterization.

In chapter 3, we introduce the physical concepts required to evaluate the photovoltaic performance. The state of the art for InGaN-based solar cells is presented as well.

Chapter 4 goes into the 2D h-BN based epitaxial liftoff technique used in this thesis to enable InGaN solar cells hybrid integration for tandem devices. The first task is to optimize the MOVPE growth of h-BN at a wafer scale. Next step consists of using 2-inch h-BN/sapphire templates for the Van der Waal (vdW) epitaxy of III-nitride device structures. Here, we present results of InGaN-based PIN and AlGaN/GaN heterostructures grown on 2-inch h-BN/sapphire wafers. The last task is the wafer-scale fabrication and the transfer of the devices to foreign substrates. In this step, we benefit from a thesis work previously done in our lab during which AlGaN/GaN HEMT gas sensors have been fully developed. Here, we fabricate these devices on 2-inch h-BN/sapphire templates and we transfer them to flexible substrates with boosted performances.

In chapter 5, we build upon the results presented previously to discuss our work about the heterogeneous integration of InGaN-based solar cells on glass with back-side reflector while enhancing performances. Here, we demonstrate the first InGaN-based

solar cells on 2-inch h-BN/sapphire wafer and their transfer to the glass substrate. III-N solar cells with various sizes and designs are processed and characterized on a full 2-inch wafer giving performances comparable to similar devices on sapphire. The subsequent crack-free transfer of the solar cells, enabled by Van der Waal bonded 2D layered h-BN, to a glass substrate with a backside reflector yields an increase in the short circuit current density of up to 20%. This demonstration of transferred InGaN-based solar cells on foreign substrates while increasing performance represents a major advance toward lightweight, low cost and high efficiency photovoltaic applications.

In the end, chapter 6 summarizes the results, perspectives and publications resulting from this work. The research perspective includes the growth of solar cells with thicker InGaN absorber using the 'semibulk' approach. This would further enhance the performances by increasing the light absorption and hence the short circuit current density. The release and transfer process could be optimized to be more reproducible especially for large scale (> 2-inch wafers). Lastly, the integration of an InGaN solar cell, as a top subcell, with lower bandgap solar cells like Si or GaAS-based devices to make a 4-terminal tandem device could be envisaged.

CHAPTER 1. INTRODUCTION

Today, 95% of PV market is based on silicon (Si) (according to IHS Markit analysts). This technology has a maximum laboratory efficiency of 26.3% [1]. This efficiency is very close to the maximum theoretical limit for a single junction (around 30 %) [2], as illustrated by the saturation in the blue curves in Figure 1-1. In order to exceed this maximum efficiency, a tandem junction is necessary. Nowadays, the record yields at the laboratory level are obtained with multi-junctions based on III-V materials, as shown in Figure 1-1. Despite their good performance, these materials have a high production cost compared to Si. Therefore, several groups have studied the integration of III-V materials with Si to realize high efficiency tandem solar cells at low cost. Recently, an InGaP / Si tandem junction was reported with an efficiency of 29.8% [4]. This efficiency is close to that of the InGaP / GaAs tandem cell with a record efficiency of a 31.6% double junction cell, realized by Alta Device [5].

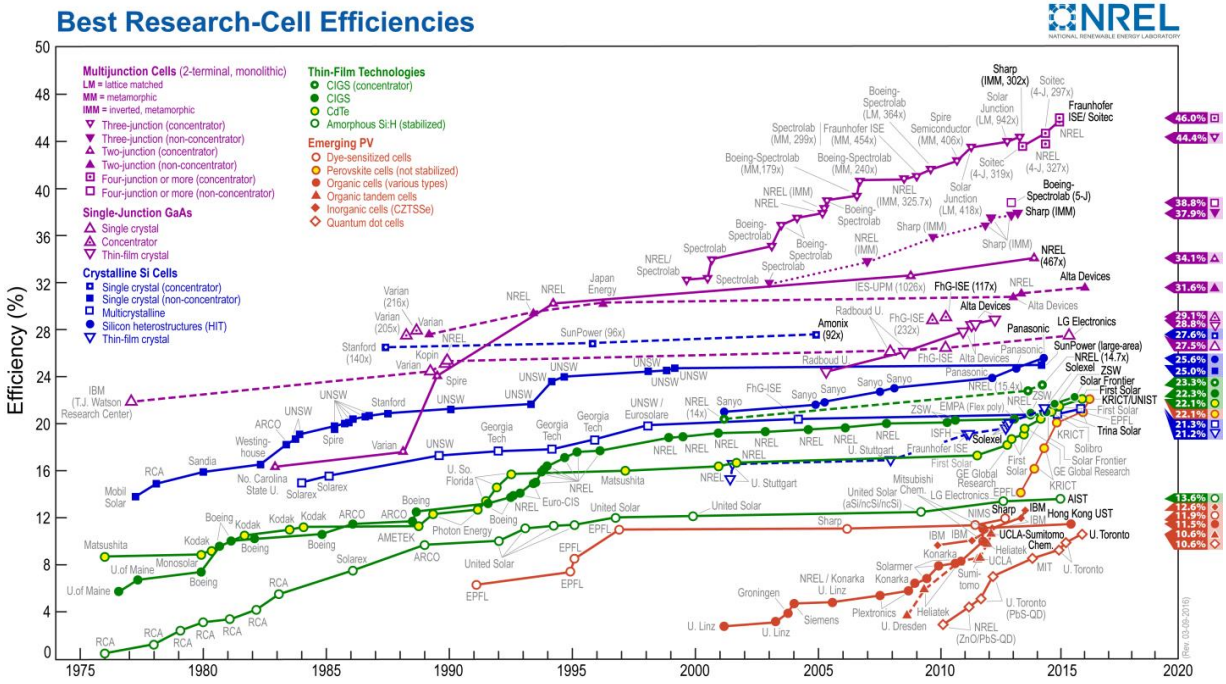

Figure 1-1 The evolution of the solar cell performance from 1977 to 2017 illustrated by NREL[3].

Similarly, InGaN can be added on top of Si to make InGaN/Si tandem solar cell. InGaN alloys have a direct bandgap that varies from 3.42 eV to 0.76 eV [6] which covers the entire solar spectrum. They have a high absorption coefficient so that a few hundred nanometers in thickness (around 200 nm) is sufficient for the absorption of the majority of incident light (more than 90%) [7]. Simulations carried out for an InGaN/Si 4-terminal tandem device predicts an efficiency around 27 % when adding a nitride solar cell with 20% In content [8]. This tandem device consists on optically bonding an InGaN cell on top of a Si cell with 4 terminals, two for each cell. One interesting way to make these hybrid systems is to grow and process the InGaN-based solar cell, release it from the growth wafer and bond it on top of a Si solar cell. Different approaches for the separation of epi-layers have been demonstrated including laser lift-off [9] and chemical etching of the growth substrate [10] or a sacrificial layer [11]. These techniques have many limitations in practice, notably high cost, long process times, and limitations in size [12][13][14]. A more recent 2D h-BN-based mechanical liftoff technique [15] has attracted much attention and has been demonstrated for some key GaN-based devices such as HEMTs (High Electron Mobility Transistors) and LEDs (Light Emitting Diodes) [16]–[18]. A few nanometers thick sp^2-bonded h-BN layer acts as a template for subsequent 3D (bulk) materials growth and also allows for the mechanical separation of the epi-layers from the growth substrate.

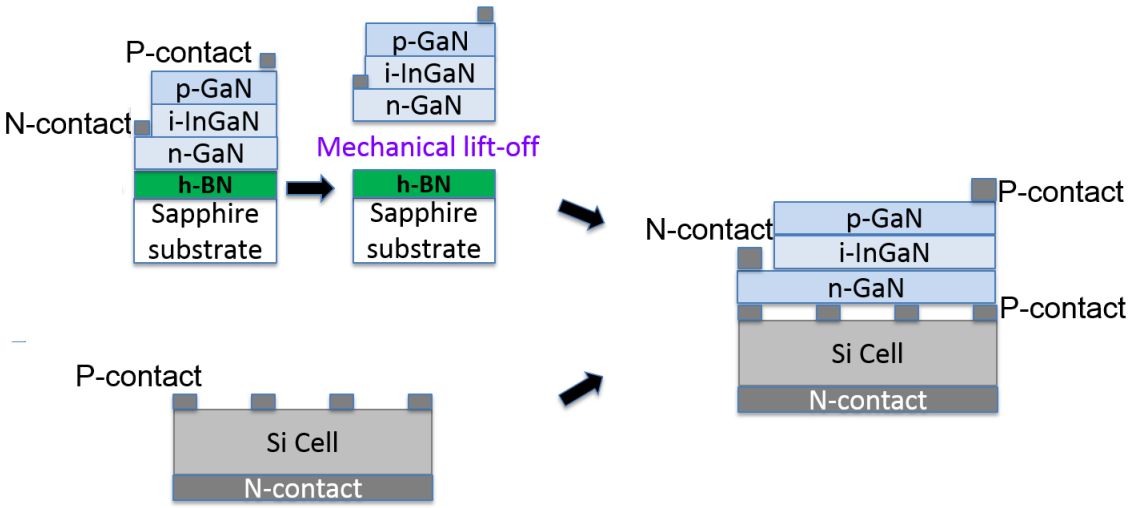

Figure 1-2 Schematic of the fabrication of a 4-terminal InGaN/Si tandem device.

The goal of this work is to develop a transfer method that allows a heterogeneous integration of InGaN solar cells with different photovoltaic technologies. This will pave the way to the fabrication of tandem devices like 4-terminal InGaN/Si solar cells, as described in Figure 1-2. For this purpose, we use a 2-inch h-BN/sapphire template to grow, fabricate and transfer InGaN-based solar cells to a glass substrate with a dielectric mirror reflecting wavelength between 400 nm and 500 nm and transmitting longer wavelength which is suitable for the operation of an InGaN/Si tandem device.

CHAPTER 2. III-NITRIDES FUNDAMENTALS AND EXPERIMENTAL TECHNIQUES

III-N nitrides are of fundamental interest for power electronics, for high frequency applications and for optoelectronics in the blue and ultraviolet spectral domains (solar cells, LEDs, Photodetectors…), due to their exceptional electronic, physical and optical properties. In this chapter we introduce some important properties of III-Nitrides, as well as the growth and characterization techniques for developing these materials.

2.1 III-Nitrides fundamentals

The III-Nitrides (III-N) materials are alloys of the elements of group III and group V of the Mendeleev table. III-N wide bandgap materials are binary, ternary and quaternary compounds formed from element III (B, Ga, Al, In) and nitrogen.

These III-N compounds can present three crystalline phases: the wurtzite (WZ), zinc blende (ZB), and rock salt [19]. The Zinc Blende phase, which consists of two face-centered cubic lattices, one occupied by the elements III and the other occupied by the atoms nitrogen, offset by a quarter of the diagonal. In the rock salt structure, each of the two atom types forms a separate face-centered cubic lattice, with the two lattices interpenetrating. The rock salt structure is only existent at high pressures. The wurtzite phase, consisting of two compact hexagonal networks, one occupied by the atoms III and the other occupied by the nitrogen atoms, shifted along the c axis by a value of 3c/8, as shown in Figure 2-1. The wurtzite phase is the most stable under normal growth conditions (on sapphire substrate, SiC, ...) [20].

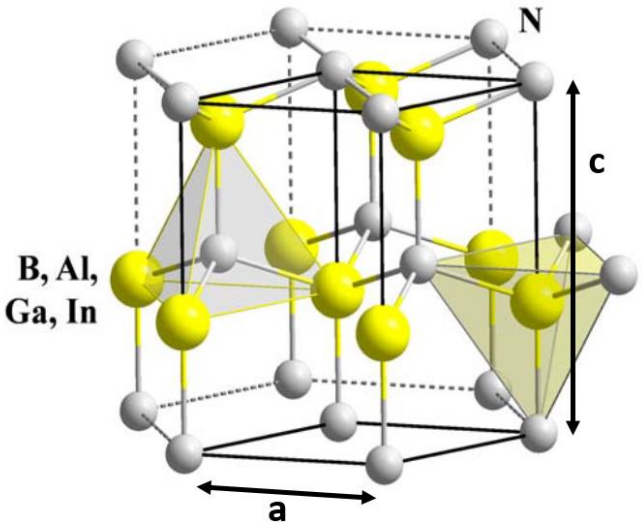

Figure 2-1Wurtzite crystal structure of III nitrides.

The III elements and nitrogen are bound by strong covalent bonds [21]. Therefore, III-nitrides are chemically and physically stable. Owing to their structure and thermal stability, III-nitrides are suitable candidates for high temperature and high-power applications. The lattice parameters and thermal expansion coefficients of BN, AlN, GaN and InN are summarized in Table 1.

Table 1– Lattice parameters and thermal expansion coefficients of III-nitrides binaries[20].

Parameters	BN	AlN	GaN	InN
a (in-plane lattice parameter) (Å)	2.55	3.122	3.189	3.548
c (out-of-plane lattice parameter) (Å)	4.17	4.982	5.185	5.718
E_g (bandgap energy) (eV)	5.9	6.28	3.42	0.7
Thermal expansion coefficients ($\Delta a/a$) ($10^{-6}K^{-1}$)	-2.7	4.15	5.59	3.8
Thermal expansion coefficients ($\Delta c/c$) ($10^{-6}K^{-1}$)	38	5.27	3.17	2.9

The in-plane lattice parameter a and the out-of-plane lattice parameter c of ternaries can be calculated by Vegard's law [22]:

$$a,c(A[x]B[1-x]N) = a,c(AN)\,.\,x + a,c(BN)\,.\,(1-x) \tag{2.1}$$

III-nitrides have wide bandgaps spanning a wide range from 0.7 (~1700 nm, infrared region) to 6.2 eV (~200 nm, deep UV region), as shown in Table 1. Especially, the InGaN covers the entire visible spectrum with a bandgap ranging from 3.42 eV to 0.76 eV [6]. The energy bandgaps of ternaries can be calculated directly from their binaries:

$$\mathrm{Eg(A[x]B[1-x]N)} = \mathrm{Eg(AN)\,.\,x + Eg(BN)\,.\,(1-x) - b\,.\,x\,.\,(1-x)} \tag{2.2}$$

In this equation, "b" represents the energy bandgap bowing parameter. Table 2 summarizes some bowing values of III-nitrides.

Table 2 – Bandgap bowing parameters of III-nitrides ternaries.

	BAlN	BGaN	AlGaN	AlInN	InGaN
Bowing (eV)	5.45[23]	9.2[24]	1[25]	2.5[25]	3[25][26]

III-nitrides display strong spontaneous polarization P_{sp} due to their wurtzite crystal structure and high degree of iconicity [27]. The polarizations of AlN, GaN and InN are summarized in Table 3.

Table 3 – Spontaneous polarization parameters from the literature.

	AlN	GaN	InN
P_{sp} (C/m^2)	-0.081[27]	-0.029[27]	-0.032[27]

According to the direction of growth, or according to the first deposited element, we will not have the same polarity [28]. If the first element is nitrogen (N), which corresponds to the direction of growth known as (0001) or direction c, we will have the last atomic layer of gallium (Ga), a polarity called Ga-face or metal-face. Otherwise, we will have an N-face polarity (000-1). Figure 2-2 shows a schematic of these two N-face and Ga-face configurations for GaN.

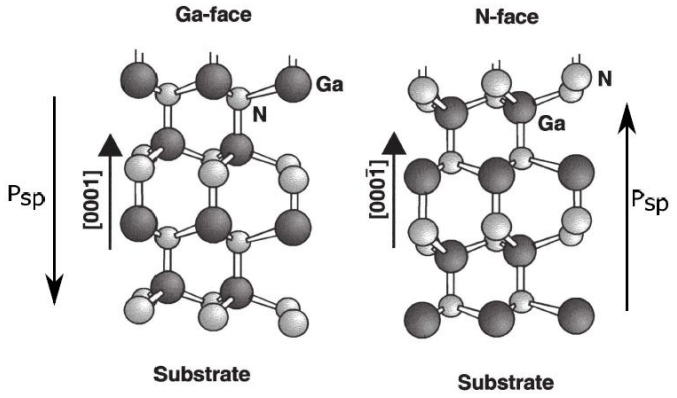

Figure 2-2 Schematic illustration of the Ga-face (left) polarity and the N-face (right) polarity for GaN[28].

For ternary alloys, the spontaneous polarization is given by:

$$\mathrm{P}sp\ (\mathrm{C}[\mathrm{x}]\mathrm{D}[1-\mathrm{x}]\mathrm{N}) = \mathrm{P}sp(\mathrm{CN})\,.\,\mathrm{x} + \mathrm{P}sp(\mathrm{DN})\,.\,(1-\mathrm{x}) - b\,.\,\mathrm{x}\,.\,(1-\mathrm{x}) \qquad (2.3)$$

Here, b is a quadratic correction term analogous to the bowing of the band gap [29]. The appropriate bowing parameters for InGaN, AlGaN, and InAlN are given in Table 4.

Table 4– Bowing parameters for spontaneous polarization in III-nitride alloys [29][30].

	InGaN	AlGaN	InAlN
b (C/m^2)	0.037	0.021	0.07

Another source of polarization is induced by mechanical stress on the epitaxial layer [27]. This polarity is called piezoelectric polarization (P_{pz}). According to the piezoelectricity, a polarity induced by this external force may be in the same direction or opposite to the spontaneous polarity, depending on the nature of the mechanical stress (compressive or tensile) [27]. The piezoelectric vector P_{pz} is parallel to the vector of the deformation, and its amplitude is given by:

$$P_{pz} = \varepsilon_x e_{31} + \varepsilon_y e_{32} + \varepsilon_z e_{33} \tag{2.4}$$

where ε_x, ε_y, and ε_z are the components of strain in the x, y, and z directions, respectively, and e_{ij} are the piezoelectric coefficients of III nitrides. In [0 0 0 1] oriented wurtzite lattices $\varepsilon_x = \varepsilon_y$ and $e_{31} = e_{32}$, and the out-of-plane strain ε_z is linked to in-plane strain ε_x through the following equation:

$$\varepsilon_z = -2 \frac{C13}{C33} \varepsilon x \tag{2.5}$$

Where C_{ij} are the elastic constants of the material [31].

Thus, the piezoelectric polarization of a III-nitride binary AN is given by:

$$P_{pz} = 2\varepsilon_x \left(e_{31} - e_{31} \frac{C13}{C33}\right) \quad (2.6)$$

The values of the piezoelectric coefficients of GaN, AlN, and InN are summarized in Table 5.

Table 5– Piezoelectric coefficients in III-nitride binaries [27][29].

	GaN	AlN	InN
e_{31} (cm^{-2})	-0.338	-0.533	-0.412
e_{31} (cm^{-2})	0.667	1.505	0.815

For ternary alloys $C_xD_{(1-x)}N$, the piezoelectric polarization is given by:

$$Ppz\,(C[x]D[1-x]N) = Ppz(CN)\,.\,x + Ppz(DN)\,.\,(1-x) \quad (2.7)$$

No bowing parameter is required in this case [27].

The total polarization can be calculated as the sum of the spontaneous polarization and the piezoelectric polarization:

$$P = Psp + Ppz \quad (2.8)$$

Here, we have reviewed some important features of the III-Nitrides. In the next section, we will present the MOVPE (Metal-Organic vapor phase epitaxy) technique that we are using in our lab to grow these materials as well as the structural, morphological and optical characterizations performed to evaluate their quality.

2.2 Experimental methods

2.2.1 Metal-organic vapor phase epitaxy (MOVPE)

Manasevit is the pioneer of the MOVPE technique [32]. During the years 1969-1975, Manasevit was able to grow by this technique gallium arsenide (GaAs), gallium phosphide (GaP), gallium aluminum arsenide (GaAlAs), gallium nitride (GaN), and aluminum nitride (AlN) [33].

The precursors used in MOVPE are mainly hydrides for the elements V and organometallics for the elements III. In case of GaN, Amonia (NH_3) can be used for precursor V and TriMethyl-Gallium (TMG) or TriEthyl-Gallium (TEG) for precursors III [34]. Dopants can be added in epitaxial layers. They come from the decomposition of many precursors, such as Silane (SiH_4) for n-type doping of GaN with Si and Bis(cyclopentadienyl)magnesium (Cp2Mg) for p-type doping of GaN with Mg.

In the MOVPE growth process, precursors and gases introduced into a chamber form a new material on the wafer surface via several steps, i.e., gas input, pyrolysis, diffusion, and surface reaction [35]. The by-products formed during these steps are pumped away with carrier gases. The general reaction for III-nitrides growth is described below:

$$R_3M_{(g)} + NH_{3(g)} \leftrightarrow MN_{(s)} + 3RH_{(g)}$$

In the above equation, M represents the group III, R the organic compound (typically an alkyl such as methyl (CH_3) or ethyl (C_2H_5)) that the group III element is attached to, and H elementary hydrogen.

MOVPE uses the properties of temperature dependence of the organometallic vapor pressure [36], as shown in equation (2.9). Thus, it is possible to transport the metal precursors to the growth chamber by simply bubbling a carrier gas (hydrogen for example) into a metal cylinder containing a liquid organometallic source maintained at a fixed temperature in a thermostatic bath (generally -10°C < T < 30°C). This container is called "bubbler". The equilibrium vapor pressure can be described by the following equation:

$$\log (P_{eq}(T)) = B - \frac{A}{T} + C \log(T) \qquad (2.9)$$

where $P_{eq}(T)$ is an equilibrium vapor pressure of the condensed phase, T is temperature in degrees Kelvin, and A, B, and C are material-specific constants. The constant C is often neglected in the practical use, making the relationship simpler.

The molar flow rate of a metalorganic source Q is a function of the flow rate of the carrier gas $F_{carrier}$ (in sccm, standard cubic centimeter per minute), the pressure P of the metalorganic source container (bubbler), and the equilibrium vapor pressure of the precursor P_{eq}. It is given by the following equation:

$$Q = (P_{eq}(T) / (P - P_{eq}(T))) \, . \, F_{carrier} / C_{STP} \qquad (2.10)$$

Where C_{STP} is equal to 22,406 cc/mole, it is the molar volume of an ideal gas at standard temperature (298.15K) and pressure (760 Torr).

MOVPE relies on the transport of chemical species in gaseous phase to the substrate raised to high temperature (500 ° C to 1300 ° C depending on the materials). In MOVPE, the pressure inside the reactor is normally between 13 mbar and atmospheric pressure.

Epitaxial materials and structures studied within this work were grown by low-pressure metal-organic vapor-phase epitaxy (LP-MOVPE) using a home-made system designed and installed by Prof. Abdallah Ougazzaden [37], as shown in Figure 2-3. The system includes four basic elements: gas handling system, reactor chamber, heating system and an exhaust (low pressure) pumping system. The temperature range is from 400 C to 1040 C and the pressure in the reactor can be regulated from 80 to 1000 mbar. Hydrogen or nitrogen can be used as carrier gas. During growth, the substrate is rotated at 60 rpm to enhance the layer homogeneity and to help maintain the laminar flow on the sample surface.

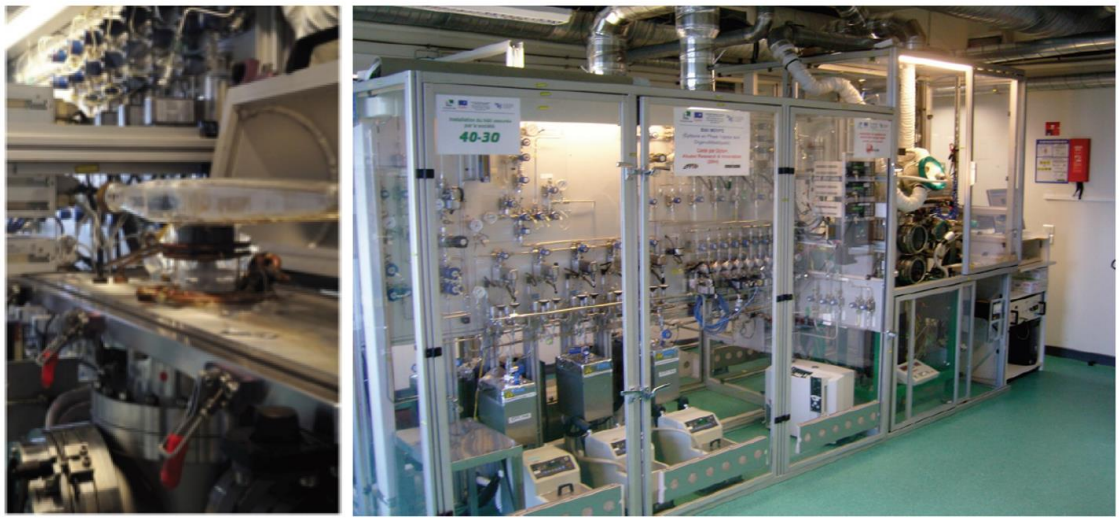

(a) Reactor chamber **(b) Gas panel**

Figure 2-3 Photographs of the reaction chamber and the gas panel of the MOVPE reactor.

An Aixtron 3x2 inch, close coupled showerhead (CCS) MOVPE system has also been brought into operation and it is shown in Figure 2-4. The surface temperature of substrates in this reactor can reach 1300 °C. This is favorable for the growth of good quality AlN/sapphire template and h-BN material.

Figure 2-4 Aixtron 3x2 inch, close coupled showerhead (CCS) MOVPE system.

Both systems are equipped with in-situ optical reflectance monitors to estimate the growth rate and get first information of the surface quality of the sample.

For the case of the T-shape reactor, a laser beam with wavelength of 633 nm is used. Interference between the reflection at the surface of thin films and reflection at the bottom causes oscillations of detected light intensity as the layer is grown. The growth rate can be calculated by the following equation:

$$\text{Growth rate} = \lambda / 2n\Delta t \tag{2.11}$$

where λ is the wavelength of the laser beam, n is refractive index of the layer and Δt is the time interval between two maxima or two minima of oscillations.

During the growth of a single layer, there would be additional light scattering due to the surface roughness. The reduced reflection intensity of maxima or minima indicates the increase of surface roughness, which can be expressed quantitatively as follows:

$$R = R_0 \cdot e^{-(4\pi\sigma/\lambda)} \tag{2.12}$$

where R_0 is the mean value of reflectance oscillations, λ is the used wavelength and σ refers to the root mean square of roughness.

2.2.2 Materials characterization techniques

- X-ray Diffraction (XRD)

X-ray diffraction (XRD) is a technique commonly used to analyse crystals and especially III-Nitrides [31]. It has the advantage of allowing a structural analysis of a material while being non-destructive. The technique is based on the elastic diffusion, without loss of energy, of a photon (electromagnetic wave) by the material. This gives rise to interferences which are more marked as the material is ordered, which is particularly favourable for our crystalline materials. The range of X-rays is interesting because the incident wavelength is of the order of the crystal lattice parameter.

The interaction of an X-ray beam with a crystal causes the diffraction of the signal in preferential directions that can be determined from Bragg's law [31]:

$$n \cdot \boldsymbol{\lambda} = 2 \cdot d \cdot \sin(\theta) \tag{2.13}$$

with d the interplanar distance, $\boldsymbol{\lambda}$ the wavelength of the incident X-ray, n the diffraction order and θ the angle of incidence as shown in the figure

In this work, high resolution XRD measurements were performed in a Panalytical X'pert Pro MRD system with Cu Kα radiation (Cu Kα1: 1.5405 Å). The height of X-ray beam from hybrid monochromator is 1.2 mm and the resolution is ~ 12 arcsec.

- Scanning transmission electron microscope (STEM)

In a scanning transmission electron microscope, a beam of electrons is transmitted through an ultra-thin specimen [38]. An image is formed from the interaction of the electrons transmitted through the specimen. Owing to the small de Broglie wavelength of electrons, this technique can resolve the lattice of atoms in the crystal. The difference of STEM from conventional TEM is that STEM focuses the electron beam into a narrow spot which is scanned over the sample in a raster, which makes it suitable for analysis such as energy dispersive X-ray (EDX) mapping, electron energy loss spectroscopy (EELS) and annular dark field imaging (ADF) allowing direct correlation of image and quantitative data. An annular dark field image, which is formed only by very high-angle and incoherently-scattered electrons, is highly sensitive to atomic number variations of the sample (Z-contrast images). By using this high-angle annular dark-field scanning transmission microscopy (HAADF-STEM), the relative intensity variations of the images reflect variations in the compositions of the material. Therefore, HAADF-STEM images can be interpreted into quantitative compositional maps by using EDX as a chemical calibration [39]. To prepare the samples for TEM characterizations, 100 nm carbon were deposited to protect the surface. Then all the thin foils were prepared using focused ion beam (FIB) thinning and ion milling by Dr. David Troadec in Institut d'Electronique de Microelectronique et de Nanotechnologie (IEMN, Lille, France). Carbon coating and HAADF-STEM characterizations in this work were performed by Dr. Gilles Patriarche in Laboratoire de Photonique et de Nanostructures (LPN, Marcoussis, France). The equipment for HAADFSTEM is aberration-corrected JEOL 2200FS electron transmission microscope.

- Energy-dispersive X-ray spectroscopy (EDX)

The energy-dispersive X-ray spectroscopy is combined with TEM technique [38]. The X-rays produced when the electron beam impacts the structure are collected and measured by an energy-dispersive spectrometer. As the energies of the X-rays are characteristic of the energy difference between the two shells and of the atomic structure

of the emitting element, EDX allows the measurement of elemental compositions of the specimen.

- Atomic force microscope (AFM)

Atomic force microscopy is a non-destructive technique to measure the sample surface in nanometer-scale resolution [40]. It consists of a cantilever with a sharp tip typically made of Si3N4 or Si. The tip radius of curvature is on the order of nanometers. When the tip is brought into proximity of a sample surface, the interaction forces between the tip and the sample cause a deflection of the cantilever according to Hook's law. This deflection can be measured by the reflection of the laser beam focused on the cantilever. The motion of the probe across the sample surface is controlled by feedback loop and a piezo-electronic scanner moving the sample under the tip.

AFM has three primary modes: tapping mode, contact mode and non-contact mode. The commonly used tapping mode maps topography by lightly tapping the surface with an oscillating probe tip. The oscillation frequency is equal or slightly lower than its resonance frequency. In order to maintain a constant oscillating amplitude, the feedback loop controls vertical position to maintain a constant tip-sample interaction. The vertical position of the scanner is stored to form the topographic image of the sample surface. In contact mode, the spring constant of the cantilever is lower than the effective spring constant holding the atoms of most solid samples together. The contact force on the tip is repulsive. The scanner gently traces the tip across the sample surface. By maintaining a constant cantilever deflection, an image of the surface is obtained. In non-contact mode, a stiff cantilever vibrates near the surface of the sample with the spacing on the order of tens to hundreds ångstroms. The surface topography can be measured by monitoring changes in the amplitude due to attractive van der Waal forces between the tip and the sample surface. The AFM images in this work were obtained by Veeco 3100 Dimension Atomic Force Microscope.

- Scanning Electron Microscope (SEM)

A scanning electron microscope is a type of electron microscope that produces images of a sample by scanning it with a focused beam of high energy electrons [41]. The electrons interact with atoms in the sample, producing signals of secondary electrons, backscattered electrons, characteristic X-rays, light (cathodoluminescence), Auger

electrons, transmitted electrons and phonons (heat). Secondary electrons are low energy electrons emitted by atoms near the surface. The number of secondary electrons depends on the angle at which the beam meets the surface of specimen. By scanning the sample and collecting the secondary electrons with a special detector, the topography of the surface can be displayed.

The SEM images in this work were obtained by Zeiss supra^{TM} 55VP. The main elements are: electron source, magnetic focusing lenses, the sample vacuum chamber, imaging system and control panel.

- Cathodoluminescence (CL)

A cathodoluminescence spectroscopy combined with SEM system is used to study optical properties of the sample [42]. The high energy electron bombardment onto a semiconductor will result in the promotion of electrons from the valence band into the conduction band, leaving behind a hole. When an electron and a hole recombine, it is possible for a photon with a specific wavelength to be emitted. The CL emission is detected via a parabolic mirror collector and analysed by a spectrometer with a focal length of 320 mm using a 1200 grooves mm^{-1} grating with a spectral resolution of 0.06 nm. The signal is then registered by a liquid N_2-cooled HORIBA JOBIN YVON Instruments Symphon 1024 x 256 CCD detector.

CHAPTER 3. INGAN-BASED SOLAR CELLS

3.1 Photovoltaic effect basis

3.1.1 The solar spectrum

In 1900 Planck proposed a new approach attesting that light is composed of energy packets, later called photons by Einstein, where each packet of energy is bound to a wavelength by the relation:

$$E_{photon} = h.\nu = \frac{h.c}{\lambda} \tag{3.1}$$

where h is Planck's constant ($\simeq 6,626.10^{-34} J \cdot s$), c is the velocity of light ($\simeq 2,998.10^{8} m / s$), and λ is the wavelength in meter.

De Broglie then showed that light can be considered both as corpuscles (packets of energy) and as an electromagnetic wave, in which the two aspects are linked by:

$$p = \frac{h}{\lambda} \tag{3.2}$$

where p is the quantity of the motion of a corpuscle.

In the field of photovoltaic (PV), we are interested in the second aspect, which attests that the light propagates in the form of packets of energy called photons. Figure 3-1 shows the intensity of light emitted by the sun as a function of wavelength, called the irradiance of the solar spectrum.

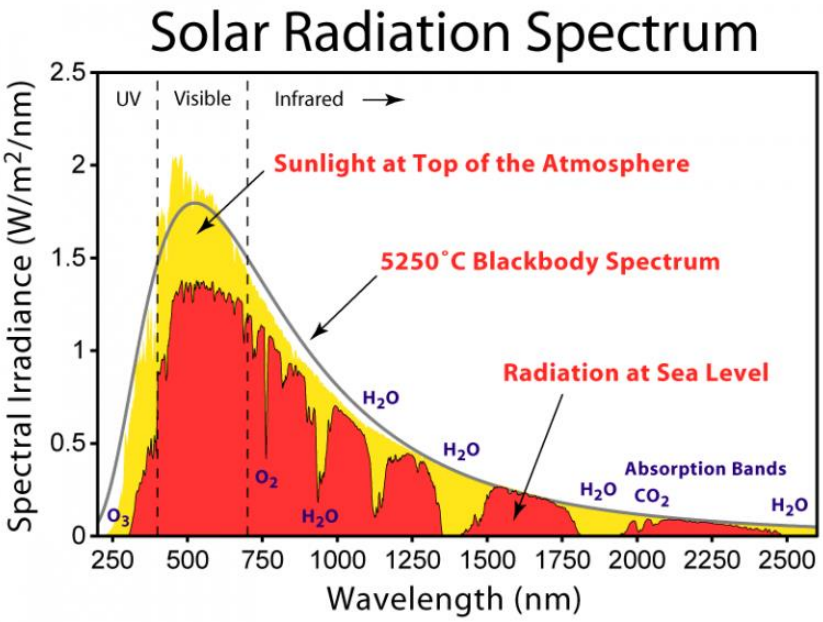

Figure 3-1 Solar radiation spectra for the incident sunlight at the top-of-the-atmosphere (yellow), at sea level (red), and a blackbody curve (black line).

The sun's irradiation passes through several layers of the atmosphere, which modifies the solar spectral irradiance according to the position in the globe. This is estimated by the mass of air through, AM (Air Mass), which is calculated by:

$$AM = \frac{1}{cos(\theta Z)} = \frac{1}{sin(\theta h)} \tag{3.3}$$

where θZ and θh are the angles of incidence with respect to the zenith and with respect to the horizon, respectively. The spectrum AM1.5, which corresponds to an angle θZ = 48.2◦, has been chosen as the standard solar spectrum for solar cell tests and the measurement of efficiencies is based on this spectrum. There exist AM1.5G and AM1.5D where the letters G and D designate the overall light beam and the direct light beam, respectively. The global beam takes into account the light beams reflected from the ground or diffused by clouds or other particles in the air, whereas the direct beam is the one that arrives directly through the atmosphere. AM1.5D is used

for testing solar cells under concentration. AM0 means that the mass of air is zero, i.e the solar spectrum outside the atmosphere.

3.1.2 Photovoltaic performances

All PV cells are characterized by certain parameters that determine their performance. Before explaining these parameters, we will first address the electrical operation of a solar cell. For a p-n junction, the relationship between the voltage at the terminals of the junction and the density of the current flowing through it is given by:

$$J = J_0 \left(\exp\left(\frac{qv}{nkT}\right) - 1 \right) \tag{3.4}$$

where V is the voltage across the junction [V], k is the Boltzmann constant (1, 38.10^{-23} $m^2.kg.s^{-2}.K$), T is the absolute temperature, n is the ideality factor is considered ideal when it is equal to 1.) J_0 is the saturation current density, also called the current density of the minority carriers, which is given by:

$$J_0 = q \cdot \left(\sqrt{\frac{Dn}{\tau n}} \cdot n_p + \sqrt{\frac{Dp}{\tau p}} \cdot p_n \right) \text{ where } n_p = \frac{ni.ni}{NA} \text{ ; } p_n = \frac{ni.ni}{ND} \tag{3.5}$$

where q is the charge of an electron ($1,6.10^{-19}$C), Dp and Dn are diffusion coefficients of electrons and holes [cm^2 / s], respectively. τ_n and τ_p are the lifetimes of electrons and holes [s], respectively. N_A and N_D are the concentrations of acceptor and donor dopants, respectively. J_0 is a determinant parameter for a p-n junction and is linked to the recombination. Indeed, the greater the recombination , the more J_0 is important and the quality of the junction is poor.

Equation (3.4) represents the relation J (V) for a p-n junction in the dark. If this junction is placed under illumination, a photo-generated current, current of minority carriers, will circulate

in the opposite direction to the current induced by the direct polarization of the junction. Then, the relation J (V) for a junction under illumination is given by:

$$J = J_0 \left(\exp\left(\frac{qv}{nkT}\right) - 1 \right) - J_L \qquad (3.6)$$

where J_L is the photo-generated current density. Figure 3-2(a) shows the equivalent electrical circuit for an ideal solar cell, modeled as a current generator with a parallel load resistor. The current across the diode depends on the source of illumination. The load resistor determines the amount of current flowing through the diode. The electrical characteristics of the solar cell under dark and illuminated conditions are given in Figure 3-2(b), with the corresponding key parameters of the solar cell.

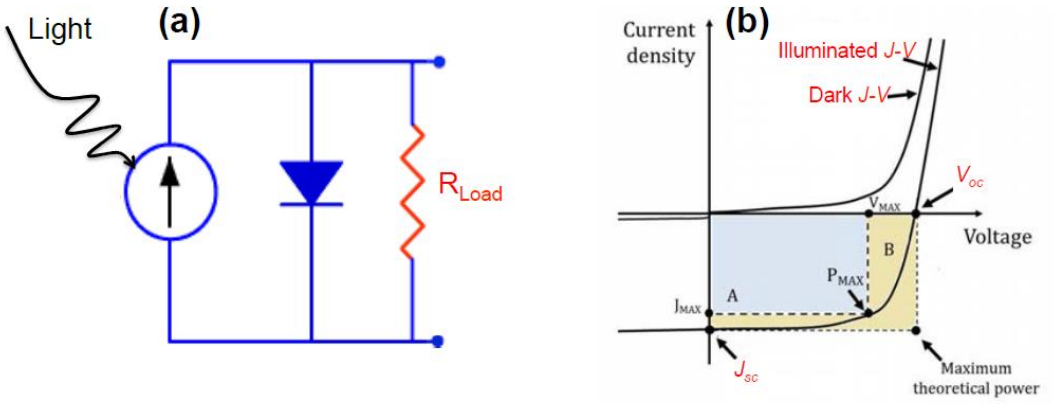

Figure 3-2 (a). Equivalent electric circuit for an ideal solar cell. The load resistance (R_{Load}) determines the amount of current across the diodes and the load, (b). Electrical characteristics of a solar cell under dark and illumination.

Four points are important in the curve J (V) for a solar cell. These are the V_{oc}, the J_{sc}, the V_{max} and the J_{max}. The V_{oc} corresponds to the open-circuit voltage of the cell, the J_{sc} is the short-circuit current density, the V_{max} and the J_{max} are the voltage and the current density at the point of the maximum power. These points are marked in Figure 3-2(b).

The J_{sc} is the maximum current through the solar cell given that the voltage across the solar cell is zero. The J_{sc} is due to the generation and collection of light-generated carriers. The J_{sc} of a solar cell is dependent on the intensity of the incident light and crystalline quality of the epitaxial layer, particularly the absorber layer. Additionally, the diffusion length and the surface recombination significantly affect the J_{sc}. In a solar cell with perfectly passivated surface and uniform generation, the equation for the J_{sc} can be approximated as:

$$J_{sc} = qG(L_n + L_p) \tag{3.7}$$

where G is the generation rate of the electron-hole pairs, and L_n and L_p are the electron and hole diffusion lengths respectively.

The V_{oc} is the maximum voltage available from a solar cell given that the there is no current across the solar cell. The V_{oc} for a solar cell can be calculated using the equation,

$$V_{oc} = \frac{nkT}{q} \ln\left(\frac{Jsc}{J0} + 1\right) \tag{3.8}$$

where *n* is the ideality factor of a diode, in-case of an ideal diode *n*=1, *kT/q* is the thermal voltage (25.85 mV at 300K), J_{sc} is the short-circuit current density and J_0 is the saturation current density.

The fill factor (FF) is the ratio between the product ($V_{max} \cdot J_{max}$) and the product ($V_{oc} \cdot J_{sc}$). This factor represents the filling ratio of the rectangle ($V_{oc} \cdot J_{sc}$) with respect to the rectangle ($V_{max} \cdot J_{max}$). This factor is given by:

$$FF = \frac{Vmax \cdot Jmax}{Voc \cdot Jsc} \tag{3.9}$$

The power conversion efficiency (PCE) is the most commonly used parameter in demonstrating the performance of the solar cell device under given source of illumination. It is defined as the ratio of energy output from the solar cell to input energy from the sun. The PCE of a solar cell is given as:

$$\eta = \frac{\mathrm{Voc} \cdot \mathrm{Jsc.FF}}{Pin} \tag{3.10}$$

where P_{in} is the incident power density which corresponds to 1 mW / cm^2 for AM1.5G.

3.2 InGaN-based solar cells: state of the art

The promising use of the InGaN alloy in the field of photovoltaic (PV) has been studied by Wu et al. (2003)[43], whereas the first experimental results were published by Jani et al (2005)[44]. This shows that these materials have only been studied for PV application for a few recent years. From the first experimental results, several challenges have been observed that limit the performance of these materials, including p-type doping as well as the epitaxial growth of a relatively thick layer of good quality. Jani et al. [44] produced two heterojunction p (GaN) -i (InGaN) -n (GaN) cells with different concentrations of indium (7% and 40%). They noticed that at 40% indium the material is much more degraded than at 7% of In for an equivalent thickness of 130 nm. By using a quantum well structure for the intrinsic region, they have been able to improve the material quality for 40% of In, but this is far from the expected performance for PV, mainly due to transmission loss and recombinations caused by a quality of degraded material. They have also noticed in the I (V) curves under light, for negative voltages, an opposite current due to the effect of an inverted diode. The latter is due to the Schottky contact formed at the interface between the metal and the p-GaN. The 7% indium p-i-n structure showed a photoluminescence (PL) emission peak corresponding to an indium composition of 27%. This is explained by a phase separation and segregation of the indium in the InGaN layer. This is

translated electrically by a reduction of (V_{oc}). Other similar structures have been reported, such as that carried out by Neufeld et al (2008) [45]. For an In composition of 12%, they obtained a V_{oc} of 1.81 V, a FF of 75% and a J_{sc} of 4.2 mA / cm^2 for an AM0 illumination under concentration. In 2011, the same group was able to have an EQE of 73% for a thickness of 60 nm of $In_{0,12}Ga_{0,98}N$ with a textured surface of 7 nm of roughness [46] EQI and FF reported in this work are 97% and 78.6%, respectively. Kuwahara et al. (2010) [47] developed an InGaN-based p-i-n solar cell with 10% indium on two different substrates, sapphire (Al2O3) and GaN. They showed that growth on a GaN substrate reduces the density of defects in the epitaxial layers. Thus, they were able to develop a non-doped absorber layer of 250 nm of InGaN. They obtained a V_{oc} of 2.23 V, a FF of 63% and a J_{sc} of 1.59 mA / cm^2 under 1.5-sun AM1.5G.

Because of the difficulty in growing a good quality and relatively thick crystalline layer for higher indium compositions, multi quantum well (MQW) and super lattice (Super Lattice SL) were used. In 2009, Dahal et al. [48] compared the performance of two p-i-n solar cells with 30% and 40% indium. The intrinsic region consists of eight periods of InGaN (3 nm) / GaN (8 nm). The V_{oc} obtained are 2 V and 1.8 V for the 30% and 40% indium cells, respectively. These values are consistent with the energy values of the gaps for these compositions (~2.32 eV and ~2.02 eV for 30% and 40% In). However, the photo-generated current density of the cell with 40% indium is worse than that of the cell with 30% indium. This is due to the degradation of the material for a higher indium composition, which was proved by PL and X-ray measurements. Liou et al. (2011) [49] reported interesting results for an InGaN-based p-i-n structure developed on a silicon substrate. They have compared the two structures p (GaN) / i (InGaN) / n (GaN) and p (GaN) / i (InGaN [3 nm] -GaN [13 nm] MQW) / n (GaN) with Indium ranging from 19% to 36%. They showed that the MQW structure exhibits higher PV performance than those obtained with p-i-n cells having a single intrinsic layer. An efficiency of 5.95% and a FF greater than 74% were achieved with the MQW p-i-n structure under illumination AM1.5. Young et al. (2013) [50]

developed a similar structure but using the super-lattice structure. The thickness of the low gap InGaN layers is equivalent to that of the previous team (3 nm) but the thickness of the large gap layers is only 4 nm. They compared the performance of the cell for several number of periods, between 10 and 50 periods. They obtained 20% of In, a V_{oc} of 2.26 V as well as a FF which can go up to 80%. However, the J_{sc} remains poor, on the order of 2 mA /cm^2, mainly due to transmission loss, due to the small thickness of InGaN. Then in 2014, the same group [51] improved their cell by adding an antireflection layer (ARC) on the front and a mirror face to increase absorption. Thus, they were able to obtain an EQE of 80% and a J_{sc} of 2.97 mA /cm^2 under illumination AM0. An increase in the power density of 37.5% compared to the cell without ARC or mirror.

In order to avoid the lattice mismatch between GaN and InGaN and the polarization effect on the hetero-interfaces in the heterostructure, other groups have tried a p-n or p-i-n homojunction structure. Jani et al. (2007) [52] demonstrated PV behavior for an InGaN-based homojunction cell with an indium composition of 28%, with which they obtained a 2.1 V V_{oc} which is consistent with its energy gap. Nevertheless, a year later they reported a 1.5 V V_{oc} for a higher gap energy (2.9 eV at In = 12%). They have shown that by adding a GaN window layer, the V_{oc} increases to 2V[53], but the current density is very low (0.04 mA /cm^2). Jampana et al. (2010) [54] reported better current density (0.91 mA /cm^2 for an indium concentration of ~15%), their structure is not quite a homojunction, the junction p-$In_{0.16}Ga_{0.84}N$ / n $In_{0.175}Ga_{0,825}N$ is inserted between a p-GaN layer and an n-GaN layer, the V_{oc} obtained is 1.73 V and the FF is 61%. Islam et al. (2013) [55] reported a homojunction structure with a high indium composition (25%). The structure consists of an n + p junction of $In_{0.25}Ga_{0.75}N$ with a total thickness of 700 nm deposited on a template layer of GaN of thickness 1 .4 μm. With this structure, they obtained a V_{oc} of 1.5 V and a J_{sc} of 0.5 mA /cm ^{2}. Cells with homojunction structure suffer from very low current density and a fill factor often degraded due to structural defects. These defects act as

recombination centers for photo-generated carriers and thus degrade the efficiency of collecting these carriers.

Some groups have studied nano-structures (e.g nano-wires, quantum dots, etc.) for the fabrication of an InGaN-based solar cell. The advantages of these structures are that they have a greater surface area of absorption, improved carrier transport and tuning of the band-gap due to the confinement properties in these structures. Due to the difficulty of obtaining good contacts and controlling the growth of these materials, few works have been able to obtain PV performances for these structures. Nguyen et al. (2011) [56] have the first cell with the nanowire structure developed on silicon (Si). The nanowires correspond to an axial p-i-n homojunction of InN. A high current density was obtained (14 mA/cm^2) under illumination AM1.5G, but the V_{oc} and the FF are very low; 0.14 V and 34.02%, respectively.

Currently, the maximum efficiency of an InGaN-based solar cell is obtained by Tran et al. (2012) for an n-InGaN / p-Si junction with an efficiency of 7.12% [57].

Recently, two new concepts have been proposed by our lab that can contribute to the advancement of these materials in the PV field. The first was reported by Pantzas et al. (2013)[58]. This approach deals with growing good quality thick InGaN absorber. It consists of periodically inserting thin GaN layers (2-3 nm) to grow a ‘’semi-bulk’’ (SB) InGaN layer. The GaN interlayers relieve strain and absorb excess In wich allows for thicker layers and higher In content. Figures 3-3 (a) and (b) show the HAADF-STEM (high-angle, annular dark field scanning transmission electron microscopy) images for two samples: the first with a bulk layer of InGaN, and the second with the semi-bulk structure. The cathodoluminescence spectra (CL) with several energies of excitation make it possible to have a profile in depth. It can be noted that for the semi-bulk structure (SB) there is only one emission peak for InGaN which is around 400nm. For the sample with a bulk layer, two distinct peaks of InGaN are observed, which means that there is phase separation in this layer.

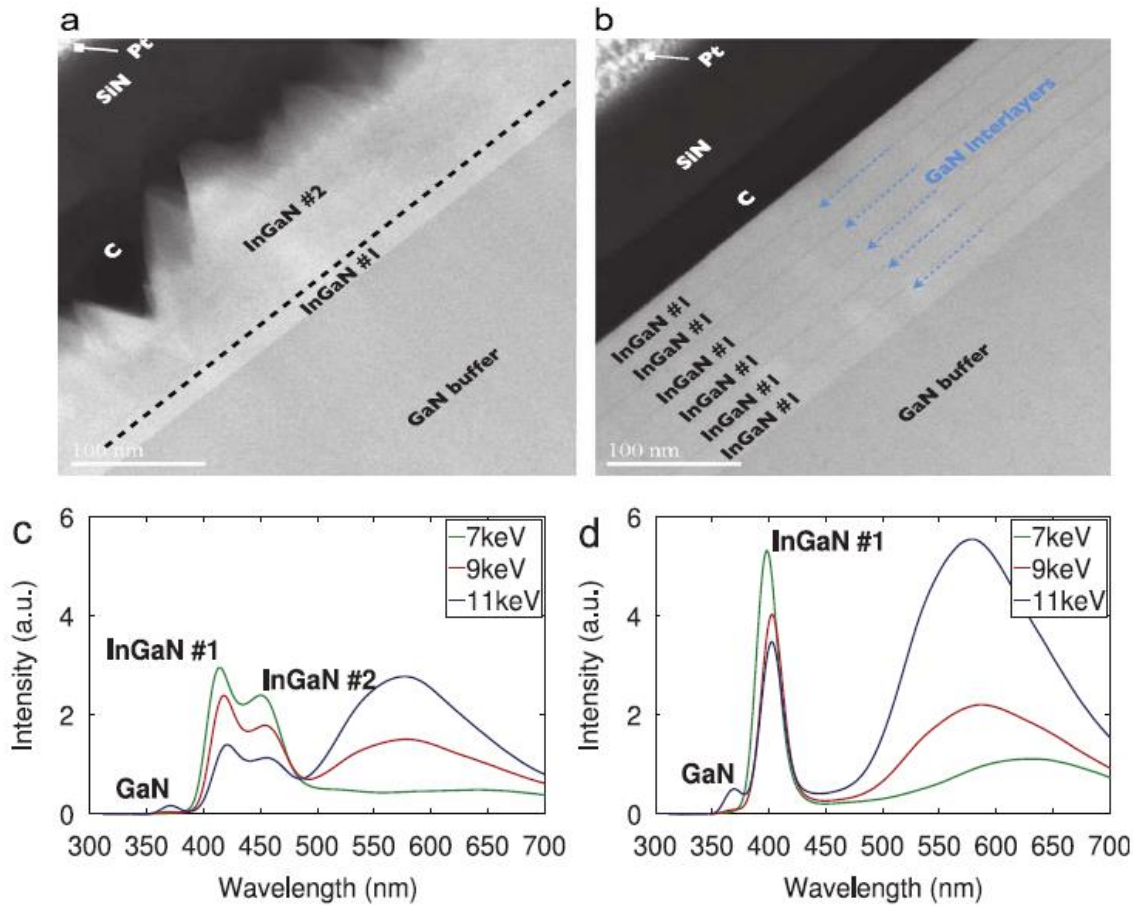

Figure 3-3 HAADF-STEM transmission electron images of (a) a bulk structure and (b)semibulk, as well as a cathodoluminiscence (CL) spectrum of (c) the bulk structure and (d) semibulk[58].

Device results for a solar cell with an $In_{0.08}Ga_{0.92}N$ semi-bulk absorber are shown in figure 3-4. Extracted efficiency, fill factor, open circuit voltage and short circuit current density are respectively equal to 0.39%, 65, 1.04 V and 0.57 mA/cm^2.

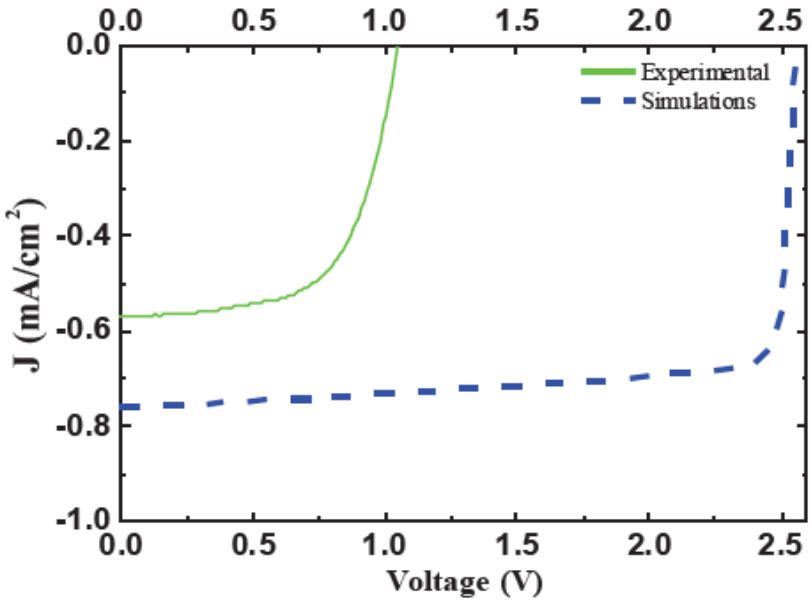

Figure 3-4 Current Density-Voltage (J − V) measured under AM 1.5G, experimentally and simulations (ideal) [59].

The second approach was proposed by Sundaram et al. (2014) [60]. The idea is to perform the growth on a selective surface. Figure 3-5 (a) shows a schematic illustration of this growth process. These hexagonal nano-pyramids have a height of 150 nm with a relatively homogeneous indium composition of 22%. Figures 3-5 (b) and (c) show a scanning electron microscopy (SEM) image of the network of these nano-pyramids and a cross-section TEM image of these nano-pyramids. The indium composition present in the nano-pyramids is twice as large as that in a plane layer constrained to the substrate under the same growth conditions. The ability to incorporate more indium without deteriorating the crystalline quality of the InGaN layers using the defect-free thick InGaN nano-structures, offers a new route to develop monolithic InGaN-based high efficiency solar cells.

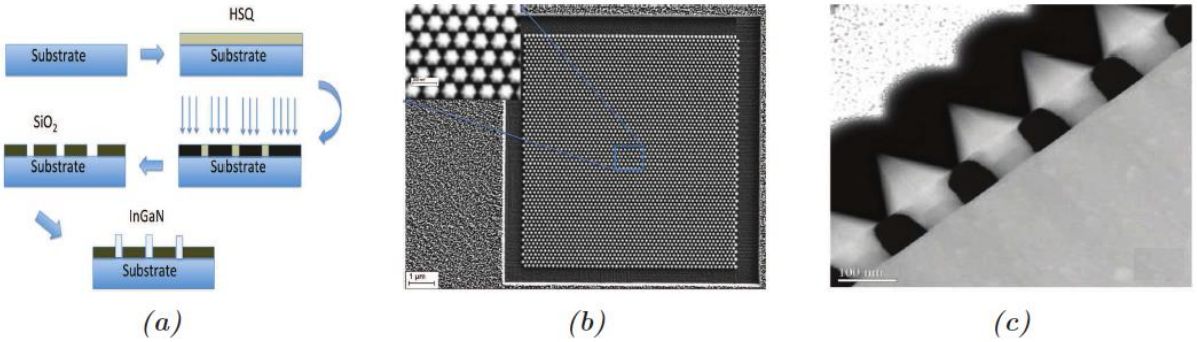

Figure 3-5 (a) Illustration of the growth process on a selective surface to develop nano-pyramids. (b) SEM image of InGaN nano-pyramid network at 22% In. (c) coss-section TEM image of the nano-pyramids[61].

CHAPTER 4. 2D H-BN EPITAXIAL LIFTOFF TECHNIQUE

The goal of this thesis is to develop a transfer method that allows the growth of InGaN-based solar cells, their fabrication and their hybrid integration with other solar cell technologies like Si-based photovoltaics. For this purpose, we have considered the 2D h-BN based transfer technique. Indeed, h-BN is a nitride material, so it is compatible with other III-Nitrides in a single growth run. Moreover, h-BN has a graphene like layered structure, so it allows the mechanical release of the above layers and their transfer to foreign substrates. In this chapter, we present the results achieved for the optimization of this transfer technique. First, the wafer-scale growth of h-BN on 2-inch sapphire wafers is presented. Then, the van der Waal epitaxy of two different device structures, an InGaN-based PIN and an AlGaN/GaN HEMT structure are discussed. Finally, the device fabrication on h-BN/sapphire template have been optimized for HEMT based gas sensors, this is the object of section 4.4.

4.1 Large-Area Two-Dimensional Layered Hexagonal Boron Nitride growth by MOVPE

4.1.1 H-BN: a III-Nitride 2D material

Boron nitride is a III-V compound that has been known for more than 170 years [62]. Unlike the other nitrides, whose most stable and most studied structure is the wurtzite phase [63], the BN presents four stable polytypes: the hexagonal BN (h-BN), the cubic BN (c-BN), wurtzite BN (w-BN) and rhombohedral BN (r-BN). While the hexagonal phase is the stable phase at atmospheric pressure, the cubic phase is stable at

high temperature [64]. The other two phases are metastable at high pressure [64]. In this thesis, we consider the BN in its hexagonal phase.

Table 5 summarizes some important properties of hexagonal Boron Nitride.

Table 5 Summary of some important physical properties of h-BN.

Parameters	h-BN
a (Å)	2.5[65]
c (Å)	6.6 [65] [66]
E_g (eV)	5.8 [67]
Thermal expansion coefficients (10^{-6}/°C)	-2.7 (‖a), 38 (⊥a)[68]
Thermal conductivity ($W.cm^{-1}K^{-1}$)	390 (‖a) [69]

The hexagonal phase (h-BN) is similar to graphene because of its 2D layered structure and very close crystalline parameters (a = 2.464 Å and c = 6.738 Å for graphene) [70]. These two compounds have a layered structure formed of the ABAB type stack of BN planes for h-BN and carbon for graphene. The hexagons formed by B and N atoms in h-BN are perfectly superimposed from one plane to another while they are shifted in the graphene, as can be seen in figures 4-1 (a) and (b). In addition, the various layers of BN are superimposed in such a way that the boron atoms of the hexagons of the lower layer face the nitrogen atoms of the upper layer. The bonds between the various planes are of Van der Waals type and they are spaced 3.3 Å apart for h-BN. The hexagons constituting the atomic layers are formed of B-N covalent bonds at a distance of 1.45 Å. The strength of the B-N link in the plane is therefore much stronger than that between the planes.

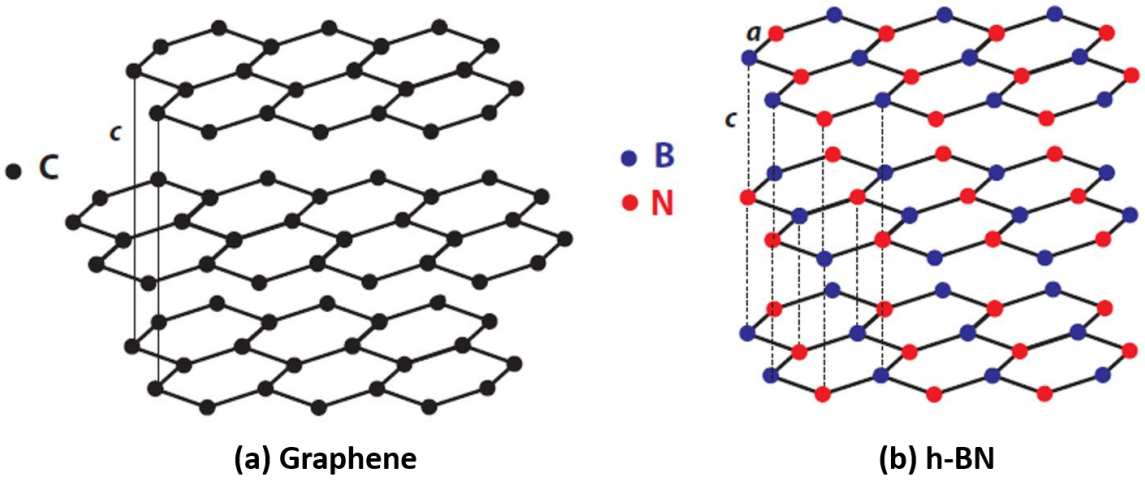

Figure 4-1 Comparison of the crystal structures of graphene (a) and hexagonal BN (b).

4.1.2 H-BN growth by MOVPE

Hexagonal BN films have been obtained by chemical vapor deposition (CVD) [71][72][73], molecular beam epitaxy (MBE) [74] or metalorganic vapor phase epitaxy (MOVPE) [75][66][76]. Most studies focused on the thick layers or several monolayers. In this thesis work, we studied wafer-scale 2D layered h-BN films that are directly grown on sapphire substrates by MOVPE.

The growth was performed in the Aixtron MOVPE CCS 3x2'' reactor using triethylboron (TEB) and ammonia (NH_3) as B and N precursors, respectively. The layers were grown at 1280 °C in hydrogen ambient at 85 mbar, with V/III ratio of about 1000. The total flow rate into the reactor is 20 SLPM (standard liter per minute). The growth rate is 15 nm/h based on the cross-section STEM characterizations.

The crystal structure of 30 nm-thick BN was examined by HR-XRD scans, as shown in figure 4-2. A clear symmetric diffraction peak is located at 26.0° that relates to

hexagonal boron nitride (0 0 0 2) crystal planes. The (0 0 0 4) plane diffract peak is also observed at 53.7°. The crystal lattice "c" is calculated to be 6.85 Å. Compared with the reported value 6.6 Å [66], the shift can be due to the residual strain in the 2D layer. The residual strain can come from the heating, epitaxy growth and cooling process. The left inset of Figure 4-2 is the HR-XRD ω-scan in the triple-axis mode to measure the mosaic width. The full-width at half maximum (FWHM) is around 684 arcsec confirming the highly oriented crystal structure along c-axis.

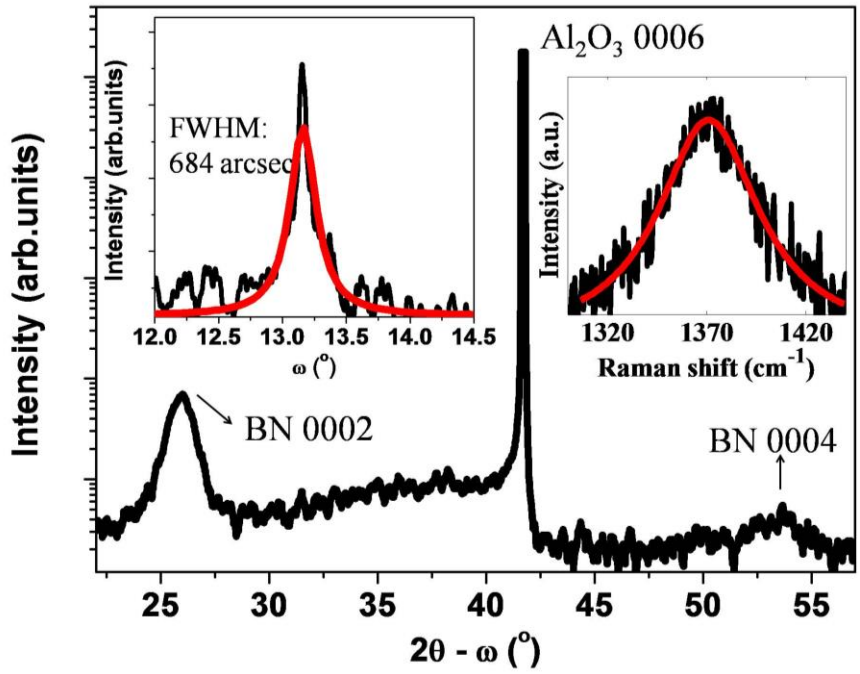

Figure 4-2 High-resolution triple axis 2θ-ω scan of h-BN grown on sapphire; left inset shows the triple axis ω-scan along with Lorentz fit (red line) of the BN (0 0 0 2) reflection and right inset shows Raman shift spectrum [77].

The hexagonal phase of the epitaxial layer is also confirmed by Raman shift measurement shown in right inset of the Figure 4-2. The spectrum of the thin BN film

fitted with Cauchy-Lorentz distribution shows a peak at 1370 cm^{-1} with the FWHM of 45 cm^{-1} that is attributed to the h-BN E_{2g} vibration mode [78].

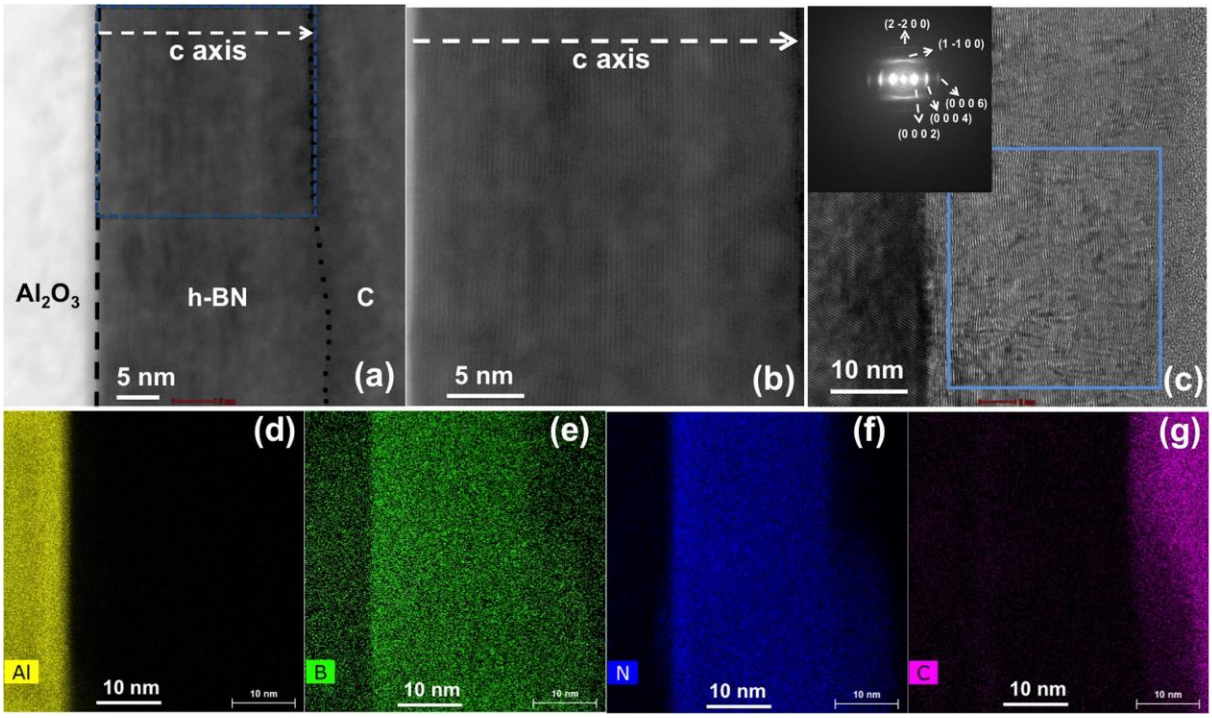

Figure 4-3 (a) Cross-section high-angle annular dark field scanning transmission microscopy (HAADF-STEM) image of 30 nm BN grown on sapphire along zone axis <1 1 -2 0>; (b) is the higher magnification image of the area marked in the box in (a) to show highly oriented lattice; (c) shows the high resolution TEM image and fast Fourier transform pattern in the inset of selected area; (d), (e), (f) and (g) are energy dispersive X-ray spectroscopy (EDX) elemental mappings of Al, B, N and C, respectively [77].

As a direct evidence of crystal phase and quality, the cross-section STEM images taken along zone axis <1 1 -2 0> are shown in figure 4-3(a) and figure 4-3 (b). The 30 nm BN layer has a highly ordered layered lattice. The stacking sequence of basal planes is clearly observed in the image with higher magnification in figure 4-3 (b) confirming that the phase of the BN layer is hexagonal rather than turbostratic or rhombohedral. The interlayer distance is 0.34 nm ($\pm$ 0.01 nm), which agrees well with the calculations from

HR-XRD. Fast Fourier transform (FFT) pattern of the high-resolution TEM image and corresponding selected area are presented in figure 4-3 (c), showing clear diffraction spots from basal planes as well as prism planes. An abrupt interface without interdiffusion between the epi-layer and the sapphire substrate and without generating any dislocations can be seen in energy dispersive X-ray spectroscopy (EDX) element mappings (figure 4-3 (d)-(g)). In the bottom part of the figure 4-3 (a), out-of-plane waviness (wrinkling) can be seen and that is due to the thermal compressive strain, since BN has a negative expansion coefficient in the plane ($a_{//}$) [79], [80]. This 2D morphology feature will be discussed in more detail in the following paragraphs.

The whole 2-inch wafer is highly transparent and demonstrates smooth surface without delamination (inset of figure 4-4). The SEM images with different magnifications are presented in figure 4-4. The flat and uniform surface can be seen in the left figure with low magnification (5kx). When looking into the image with 20 kx magnification in figure 4-4 (b), the hexagonal wrinkle pattern is observed and the average wrinkle spacing is around 400 nm. The majority of wrinkle junctions (>90%) are threefold to form oriented honeycomb pattern indicating it is under isotropic biaxial compression strain[81]. This wrinkle pattern is a ubiquitous phenomenon for deformed graphene due to its low bending rigidity [81], [82] , and was also observed in h-BN monolayer flakes deposited by CVD [80], [83], [84].

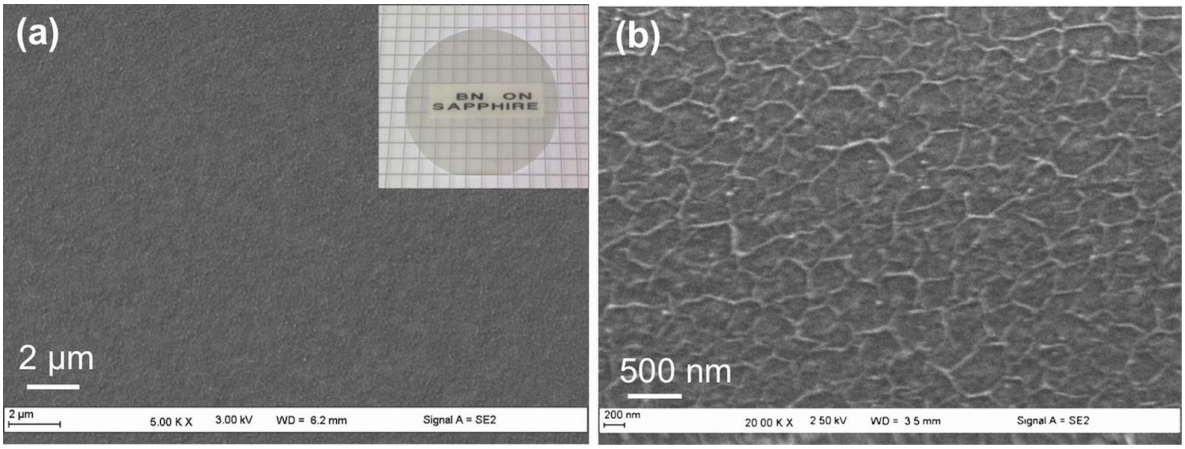

Figure 4-4 Scanning electron microscope images of BN grown on sapphire (a) with low magnification to show uniform smooth surface and (b) with higher magnification to show hexagonal wrinkle pattern; inset of (a) shows the transparent 2-inch wafer after growth [77].

The morphology change of the BN layers with different thicknesses is shown in figure 4-5. Compared with the sapphire substrate in figure 4-5 (a), the surface of 3 nm-thick BN layer in figure 4-5 (b) is flat showing growth step feature. This morphology also indicates that step-flow growth mode is dominant here to form flat surface. When the layer thickness is 30 nm, the localized wrinkles appear. AFM characterization in figure 4-5 (e) provides detailed morphology of 30 nm BN. An example of the profile across one wrinkle along the line marked in the figure 4-5 (e) shows that it is 8 nm high. In fact, the height of different wrinkles can vary from 5 nm to 10 nm. Then, when the layer thickness is increased to 60 nm, the wrinkle height increases as well, ranging from 15 nm to 25 nm.

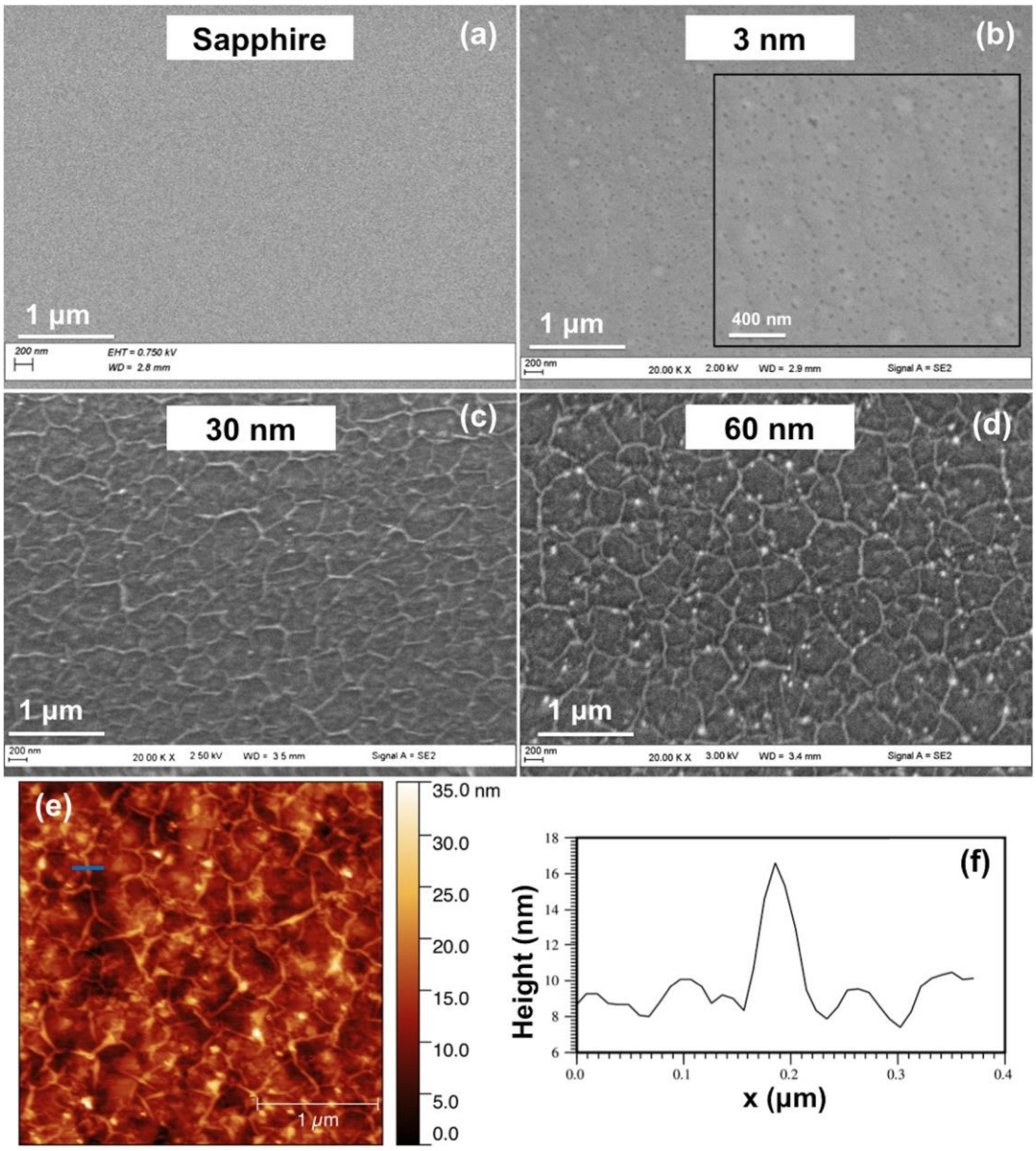

Figure 4-5 (a), (b), (c) and (d) are SEM images of the sapphire and of the 2D BN layers with different thickness; (e) is AFM characterization of 30 nm BN layer in (c) ; (f) height profile across the wrinkle along the blue line marked in (e)[77].

4.2 Van Der Waal epitaxy of III-Nitrides on 2D h-BN

Van der Waal epitaxy (vdWE) has been first introduced by Koma et al. [85] [86]. As opposed to standard epitaxy, this technique occurs when the epitaxial crystalline layer is bound primarily to the substrate by weak Van der Waals interactions; Figure 4-6 illustrates this difference. Thus, vdWE is different from conventional epitaxy, which has strong chemical bonds connecting the epitaxial material and the substrate at the interface. Various advantageous arise in vdWE including the possibility to grow well-crystallized epitaxial material without any necessity to satisfy lattice matching requirement with the substrate. To allow the growth via vdWE instead of via conventional heteroepitaxy, Koma and co-workers originally suggested the usage of overlayers and substrates from materials whose surface is free of active dangling bonds [87], such as 2D h-BN.

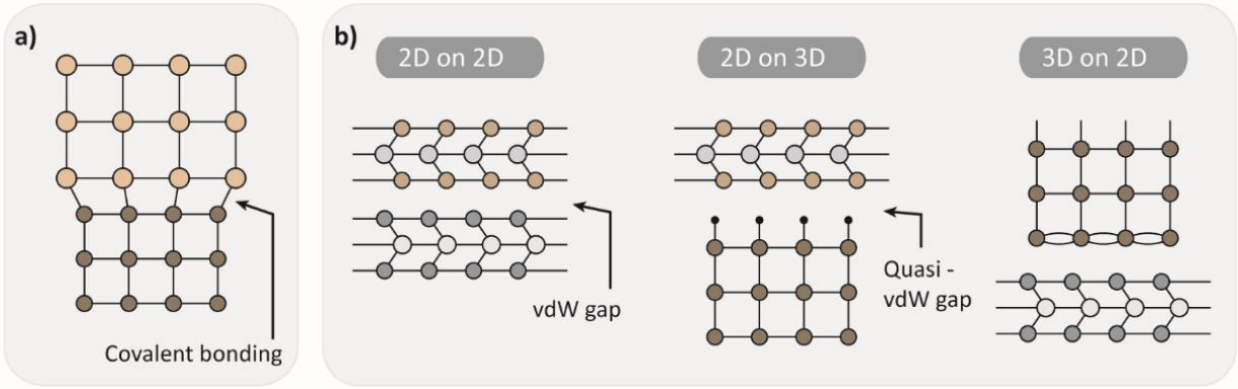

Figure 4-6 Illustration showing the (a) covalent bond formation during standard epitaxy of 3D material on 3D substrates and (b) the different combinations of material stacking for van der Waals epitaxy [88].

For this thesis, we use 2D h-BN/sapphire templates for the vdWE of sp^3-bonded GaN-based alloys. Two structures have been investigated, a MQW (multi quantum well) InGaN based PIN and an AlGaN/GaN heterostructure.

4.2.1 InGaN based PIN on h-BN

The growth optimization of 2D-layered h-BN on a 2 inch sapphire substrate has enabled us to investigate vdWE of InGaN/GaN MQW structure on a 3 to 5-nm thick 2D h-BN layer and subsequent exfoliation from the sapphire substrate [17]. The growth was performed in the Aixtron MOVPE CCS 3x2'' system on (0001) sapphire substrate. Triethylboron (TEB), Trimethylgallium/Triethylgallium (TMGa/TEG), Trimethylindium (TMIn) Trimethylaluminum (TMAl) and Ammonia (NH_3), were used as B, Ga, In, Al and N sources respectively. Silane (SiH4) and Cp_2Mg was used as n-type and p-type doping sources.

First, a h-BN layer (3-5 nm) was grown on the sapphire substrate at 1280°C. The thickness of this layer was carefully chosen to optimize the GaN quality on top. Snure et al. have reported in [89] that the smoothness of the h-BN surface affect the quality of the above GaN layer. Based on that we have studied the growth of 300 nm GaN template on h-BN/sapphire using a 250 nm $Al_{0.14}Ga_{0.86}N$ nucleation layer. Here, we have considered three different thicknesses of the h-BN layer: 1.5 nm h-BN (RMS roughness = 0.342 nm over 5x5 μm^2), 3-5 nm h-BN (RMS roughness = 0.732 nm over 5x5 μm^2) and 20 nm h-BN (RMS roughness = 2.956 nm over 5x5 μm^2). The SEM images of the GaN surface and the FWHM of (002) rocking curves shown in Figure 4-7 suggest that 3-5 nm is the optimal thickness for the h-BN layer.

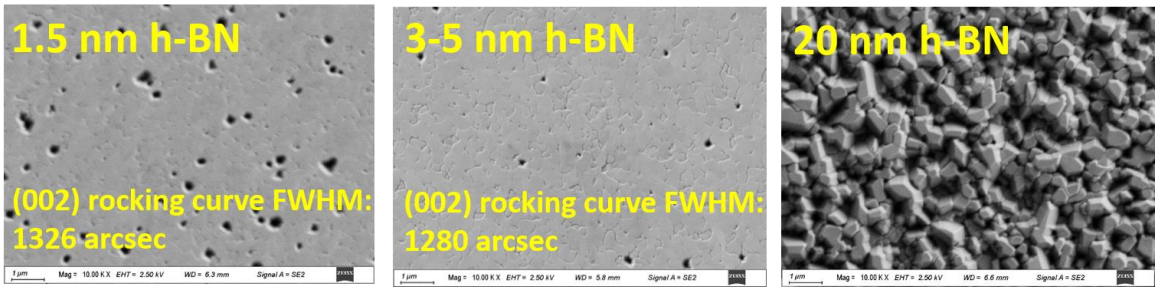

Figure 4-7 SEM images and XRD (002) FWHM rocking curves of 300 nm thick GaN layers grown on 1.5, 3-5 and 20 nm h-BN layers.

Then, an intermediate Si-doped AlGaN layer (250 nm) with an Al mole fraction of 14% was grown at 1100°C. This layer acts as an interfacial buffer between sp^3-bonded 3D epitaxial films and 2D h-BN and promotes nucleation [90]. As shown in Figure 4-8, GaN does not wet the h-BN layer so we had to include some Al for a better wetting.

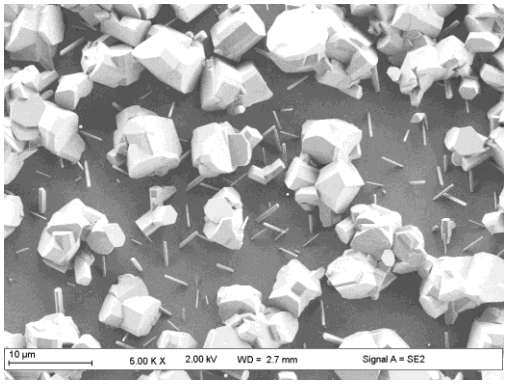

Figure 4-8 SEM image of GaN directly grown on 3 nm h-BN layer.

The InGaN/GaN MQW structure consists of a Si-doped GaN layer (0.5 µm), 5-periods of InGaN/GaN multi-quantum wells (MQWs), and a Mg-doped GaN layer (0.25 µm). The MQW structure consists of a 12-nm-thick GaN barrier layer and a 2.5-nm-thick InGaN quantum well layer with an In mole fraction of 15%. The electron and hole carrier concentrations in the Si- and Mg-doped GaN layers are 5×10^{18} and 1×10^{17} cm^{-3}, respectively. Figure 4-9(a) and (b) show the schematic of the grown structure and the wafer photograph after growth, respectively. Additionally, two similar MQW structures have been grown under the same conditions: the first directly on sapphire without the h-BN layer and the second on a conventional 1.5 µm thick GaN template on sapphire.

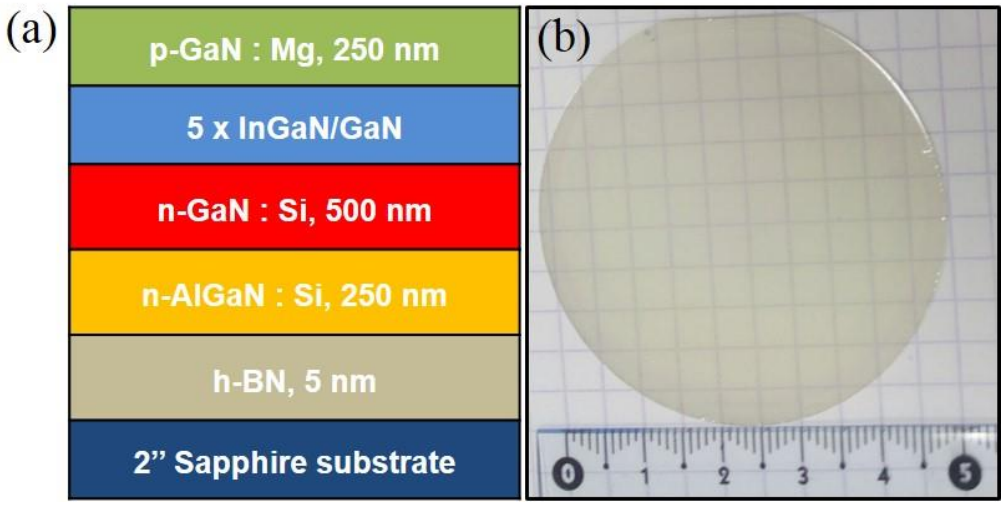

Figure 4-9 (a) Schematic illustration of the grown structure and (b) the resulting transparent wafer photograph after epi-growth.

The crystallographic properties of the MQW structure on h-BN in comparison with the MQW structure on a conventional GaN template were analyzed by High Resolution X-ray Diffraction (HR-XRD) using 2θ–ω configuration, the rocking curve scans are shown in Figure 4-10.

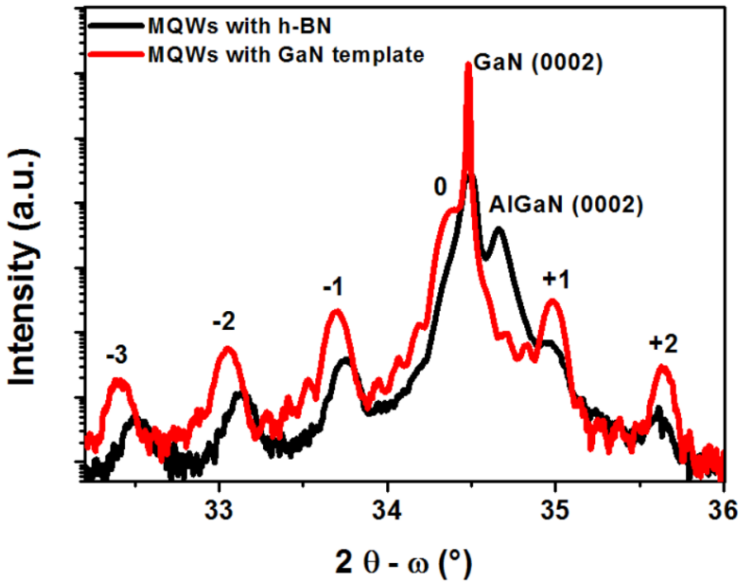

Figure 4-10 High resolution X-ray diffraction 2θ - ω scans of the MQW structure on the h-BN layer and the same structure using conventional GaN template.

In the case of MQW structure on conventional GaN template, one can observe the intense GaN peak and satellite peaks from the MQWs up to the third order with (n-2 = 3) pendellosung fringes indicating good periodicity and abrupt interfaces in the quantum wells. For the MQWs sample with h-BN layer, the satellite peaks from the MQWs up to the third order were also observed, along with GaN (0002) and AlGaN (0002) diffraction planes. The difference in the diffraction peaks intensity may be attributed to the thickness of the GaN which is lower in case of the device structures grown on h-BN. SEM images, shown in Figure 4-11 (a) and (b), confirm that surface quality of the sample with h-BN layer is similar to the one with conventional GaN template. Atomic Force Microscopy (AFM) measurements on the p-GaN surface for both cases, gave a comparable RMS roughness around 1.6 nm over a 5 µm x 5 µm area. Concerning the MQW structure on sapphire without the h-BN layer no x-ray diffraction peaks were observed, even from GaN, and SEM image of the surface showed completely 3D layers. This confirms that the h-BN acts as an effective buffer layer.

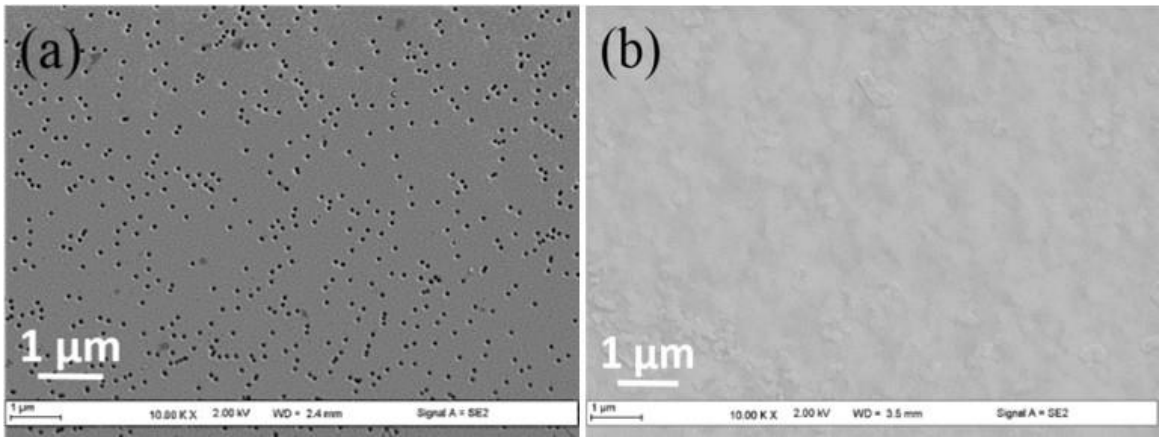

Figure 4-11 SEM images of the MQW structure surface (a) on conventional GaN template and (b) on h-BN.

4.2.2 AlGaN/GaN structure on h-BN

AlGaN/GaN structure was grown by MOVPE on 2-inch h-BN/sapphire substrates (Figure 4-12 a). The grown structure is shown in the inset of figure 4-12 b. The high-resolution X-ray diffraction (HRXRD) $2\theta - \omega$ scan of the grown layers on h-BN/sapphire is presented in figure 4-12 b. The satellite peaks from the $Al_{0.25}Ga_{0.75}N$/GaN heterostructure were clearly observed, along with GaN (002) and $Al_{0.14}Ga_{0.86}N$ (002) diffraction planes. Simulation, shown in blue, confirms the Al content and the thicknesses of the different layers in the structure. The broadness and the low intensity of the AlGaN buffer compared to the simulated one are due to the 3D morphology of this layer as shown in the elemental EDX mapping of Al in figure 4-12 d. The high resolution TEM image in figure 4-12 c is a direct evidence of the crystal phase and quality of the 5-nm thick h-BN layer. An abrupt interface without inter-diffusion along the $Al_{0.25}GaN_{0.75}$/GaN can be seen in energy dispersive X-ray spectroscopy (EDX) element mapping in figure 4-12 d.

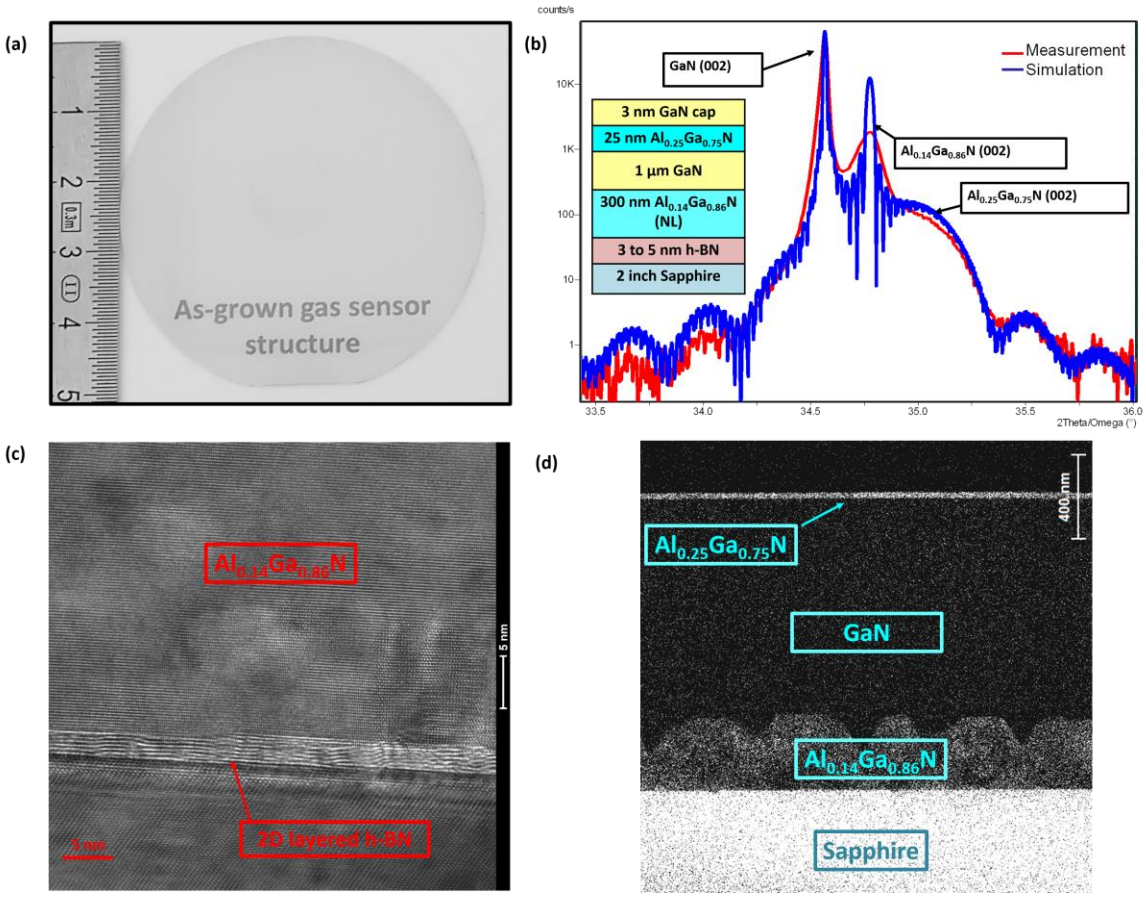

Figure 4-12 (a) Photo of the grown AlGaN/GaN on h-BN, (b) High resolution X-ray diffraction 2θ - ω scans of the grown AlGaN/GaN heterostructure on h-BN using $Al_{0.14}Ga_{0.86}N$ as a nucleation layer (NL), the red curve is the measurement and the blue curve presents the simulation result. The inset is a schematic of the grown structure. (c) High resolution TEM image showing the interface between the 2D layered h-BN and the AlGaN nucleation layer. (d) Energy dispersive X-ray spectroscopy (EDX) elemental mapping of Al.

4.3 Wafer-scale release of InGaN MQW based PIN with commercial tape

After demonstrating the wafer-scale growth feasibility of GaN-based materials on 2D h-BN, a subsequent release of the InGaN MQW structure from the 2-inch sapphire substrate using an adhesive tape was attempted. The atoms within a mono-layer of h-BN are bound by chemical bonds. However, adjacent mono-layers are connected only by weak van der Waals attractions, which is the reason why layered materials can be exfoliated with ease. Figure 4-13 (a) and (b) show photos of two MQW structures lifted

off using an acrylic conductive adhesive layer on an aluminum foil and a copper foil, respectively. The entire MQW structure was exfoliated from the 2-inch substrate with excellent reproducibility.

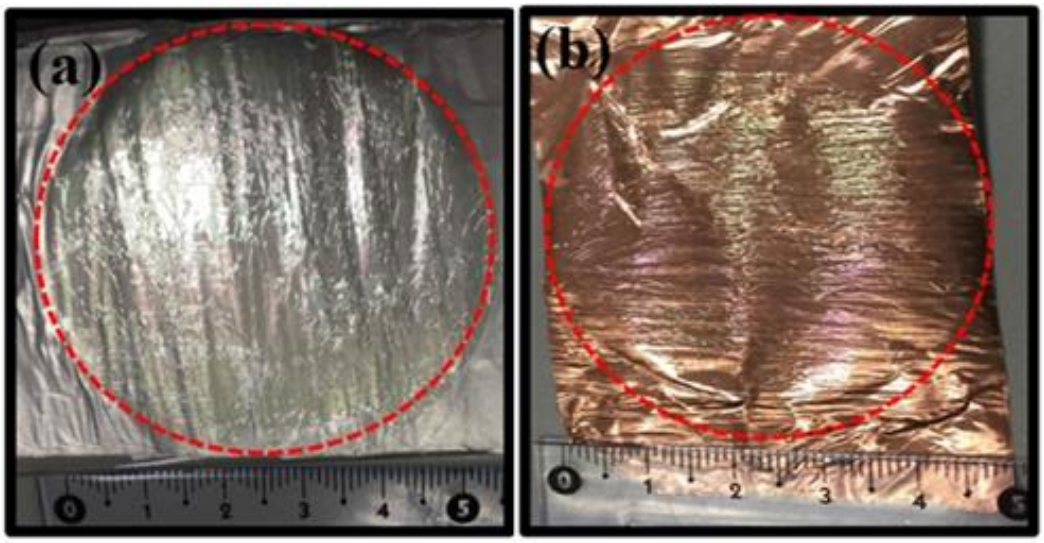

Figure 4-13 Photograph of the MQW structure after exfoliation using (a) an aluminum foil and (b) a copper foil.

Structural characteristics of the released wafer were studied to check for degradation due to lift-off. The 2θ - ω scans of the MQW structure after the release, in comparison with before lift-off are shown in figure 4-14. The scans exhibit clearly the signature satellite peaks of the MQW structure, providing evidence that the structural integrity is conserved. The lower intensity of the satellite peaks after the lift-off can be explained by the thicker stack (750 nm) of AlGaN and GaN layer traversed by x-rays before reaching the MQW stack, since after lift-off the structure is flipped upside down.

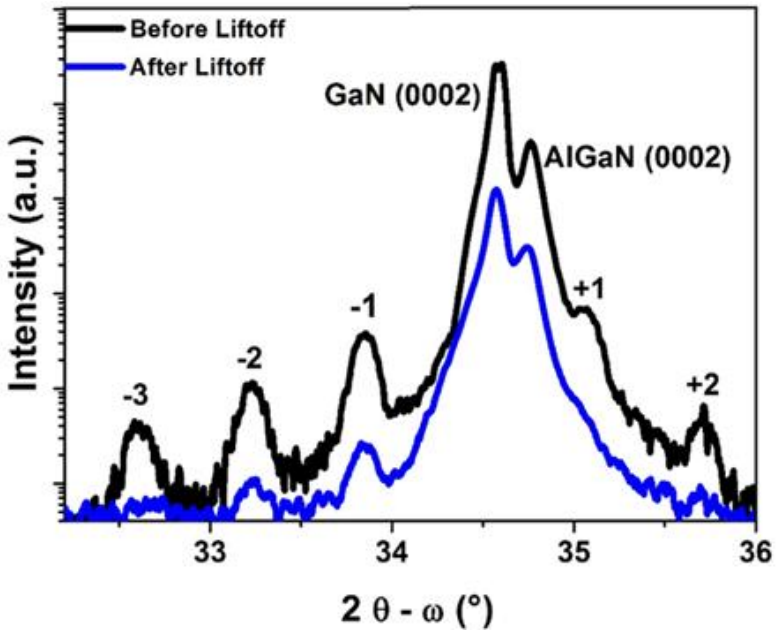

Figure 4-14 X-ray diffraction using the 2θ - ω configuration of the MQW structure before and after the transfer.

The separated surface morphology of the lifted-off MQW structure has been investigated with SEM and AFM. Figure 4-15 (a) shows the SEM image of the n-type buffer surface in the released MQW structure, which exhibits smooth surface morphology. From the AFM image, RMS roughness of 1.14 nm over a 5 µm x 5 µm area was obtained. This smooth surface indicates that the exfoliation occurred by breaking the bonds between the 2D layered BN layers and not at the interfaces of the sp^3 bonded III-nitride layers which would result in a surface with increased roughness. Theoretical investigation in the literature using density functional theory (DFT) and the registry index model also shows that the transfer happens within the BN 2D layers which exhibits the minimum energy barrier of 2 meV/atom required to separate a BN/BN bilayer [91]. The surface of the sapphire after lift-off has been investigated by AFM and steps of less than 3 nm between islands of BN and the surface has been measured confirming the separation within the BN layer.

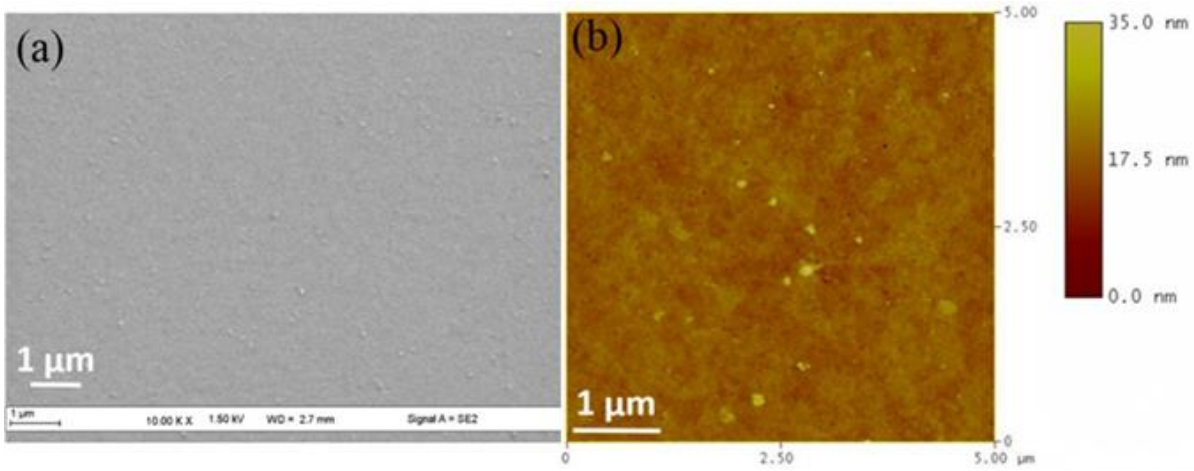

Figure 4-15 (a) SEM image of the BN/AlGaN surface in the MQW structure and (b) AFM image of the BN/AlGaN separated surface in the MQW structure.

Optical characteristics of the MQW structure have also been investigated. Depth resolved cathodoluminescence (CL) spectra for the MQW structure before and after exfoliation from the sapphire substrate recorded at room temperature with an electron beam excitation energy of 17 kV are shown in figure 4-16 (a), (b). Before lift-off, the MQW structure exhibits the GaN near band edge emission peak at 364 nm, and the MQW emission peak at 454 nm which corresponds to 15% In content in the quantum wells. After lift-off, emission from the InGaN/GaN MQWs is observed at 458 nm, as shown in figure 4-16 (a). The red-shifted peak position can be due to a partial residual strain relaxation in the active region after lift-off. The same intensity ratio of 1.1 between the GaN and the MQWs peaks before and after the lift-off has been observed. The magnitude of the two main peaks' intensity before and after the liftoff is different by only 15%. This could be attributed to a slight difference in the experimental conditions. The two shoulders around the MQWs peak in the CL spectrum after lift-off, presented in figure 4-14 (a), can be explained by the Fabry-Perot effect. Figure 4-16 (b) shows the CL spectrum observed by exciting from the n-side of the lifted off surface which clearly exhibits the AlGaN and GaN peaks with a less intense peak from MQWs. The presence of AlGaN and GaN peaks throughout the exfoliated sample is consistent with exfoliation occurring at the BN.

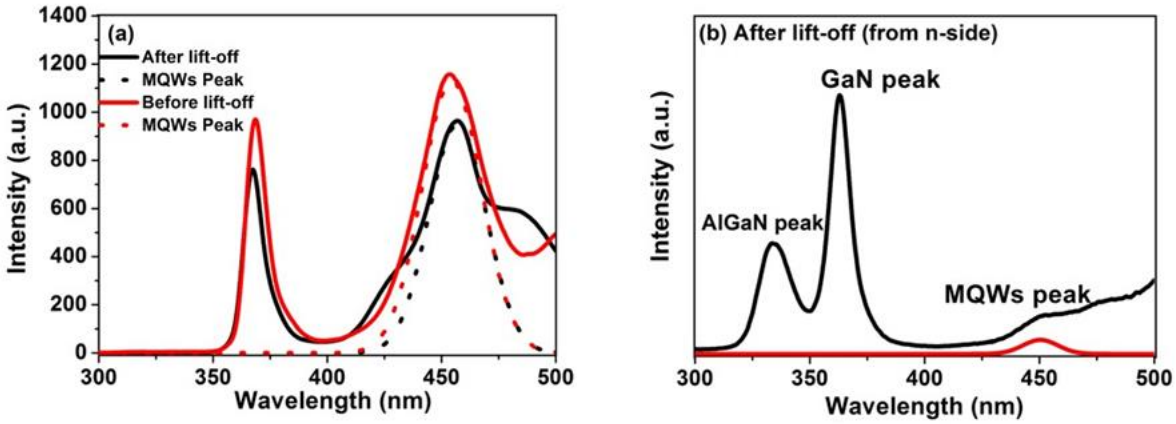

Figure 4-16 CL spectrum recorded at room temperature under excitation of 17 kV (a) before and after lift-off (excited from the p-doped layer) with fitted MQWs peaks in dotted lines and (b) after lift-off (excited from the n-doped layer) with fitted MQW peak in red.

This series of studies confirm that the structural and optical characteristics are preserved during this exfoliation process. Probe tips were placed to obtain electroluminescence from the MQW structure. Figure 4-17 shows a graphical representation of the probing configuration and a camera image of the blue light emitted from the exfoliated layers by electrical injection without metal contact deposition.

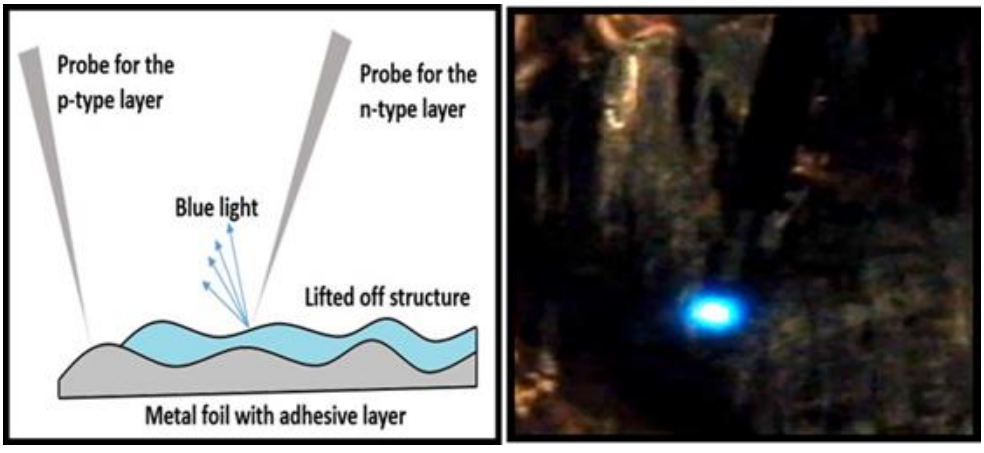

Figure 4-17 Blue light emission by electrical injection from the exfoliated MQW structure.

4.4 Wafer-scale device fabrication and transfer: HEMT (High Electron Mobility Transistor)-based gas sensors on flexible substrates

In the previous sections, we have demonstrated the vdWE of GaN-based device structures on 2-inch h-BN/sapphire templates. We have also confirmed the feasibility of the 2D h-BN enabled transfer method at a wafer-scale by exfoliating the InGaN MQW PIN structure and showing the conservation of the structure properties after liftoff. Now, we need to move forward to optimize the device fabrication using h-BN/sapphire templates and demonstrate a complete transfer on a foreign substrate. For this purpose, we have considered the AlGaN/GaN structure to fabricate HEMT (High Electron Mobility Transistor)-based gas sensors [92]. These devices has been already developed in our lab during a thesis work [93], more details about their operation principle can be found in Appendix C.

HEMT-based gas sensors with catalytically active gate electrodes are an interesting sensing technology due to their many advantageous material properties, such as high thermal and chemical stability [94], which have demonstrated sensitivity and suitability for detection of diesel exhaust gases[92][95]. With appropriate transfer technique, HEMT sensors have promising potential to be integrated into wearable applications. This would enable the development of a wearable and portable air pollutant monitoring platform to collect air pollutant data (species and concentration) continuously. Such a system requires inexpensive, miniaturized (micro-scale), rapidly responding and highly sensitive gas sensors that can be operated on malleable and lightweight substrates.

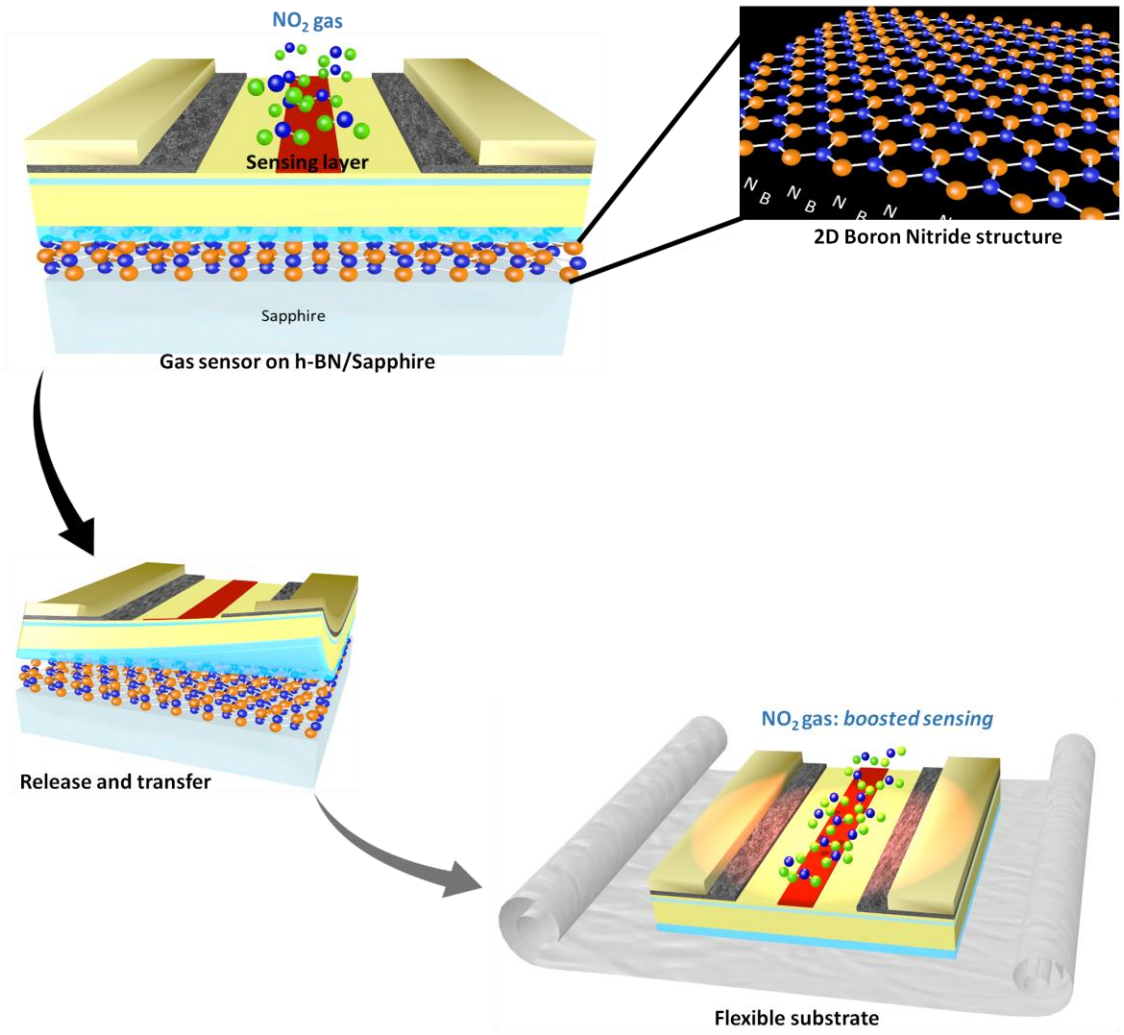

Figure 4-18 Our approach for the growth, fabrication, release and transfer of boosted AlGaN/GaN gas sensor to a flexible sheet using h-BN as a buffer and release layer.

The mechanism for gas sensor operating on a foreign substrate like a flexible carrier is illustrated in Figure 4-18. The 2D h-BN layer enables the release of the device and its transfer to an acrylic adhesive layer. This layer is expected to confine the heat generated by self-heating, leading to higher operating temperature of the gas sensor, which is known to contribute to an increase of the sensitivity and an improvement of the response time [92].

4.4.1 Electrical characterization of AlGaN/GaN devices on h-BN sapphire

The process fabrication has been adapted for device structures on 2D h-BN. For instance, no ultrasonic cleaning is used, rapid thermal annealing conditions such as gas flow rate and temperature ramping were optimized, and contact with liquids was limited during each step to prevent spontaneous delamination. The source, drain, and contacts were defined by optical lithography. The deposit of the source and drain metallization contact structure consisted of electron beam evaporated Ti/Al/Ni/Au (12/200/40/100 nm) multilayers followed by a rapid thermal annealing at 870°C for 30s under nitrogen atmosphere. The gate contact was deposited using Pt sputtering with a thickness of 15 to 20nm at a pressure of 6mTorr, providing a catalytically active sensing layer. Gate dimensions are Lg=2µm and Wg=200µm, with a total drain to source spacing of 6µm. Electron beam evaporated Ti/Al/Ni/Au (12/200/40/100 nm) pads were deposited to facilitate electrical contacting of the devices.

The resulting processed devices are shown in Figure 4-19 a. Transfer length measurements (TLM) performed on several locations of the wafer show an average specific contact resistivity of $3x10^{-5}$ $\Omega.cm^{-2}$, indicating good ohmic contact behavior. Wafer mapping of the current-voltage characteristics reveal more than 1000 functional HEMT devices on the 2-inch wafer (Fig 4-19 b and 4-19 c). We also note that more than 100 devices exhibit more than 70% gate pinching, which we have quantified as $[I_{ds}\ (V_{gs}=0V)-I_{ds}(V_{gs}=-6V)/\ I_{ds}(V_{gs}=0V)]*100$ at $V_{ds}=10V$. This is a direct indication that these devices have good control of the carrier concentration in the 2DEG by the gate contact (Figure 4-19 d).

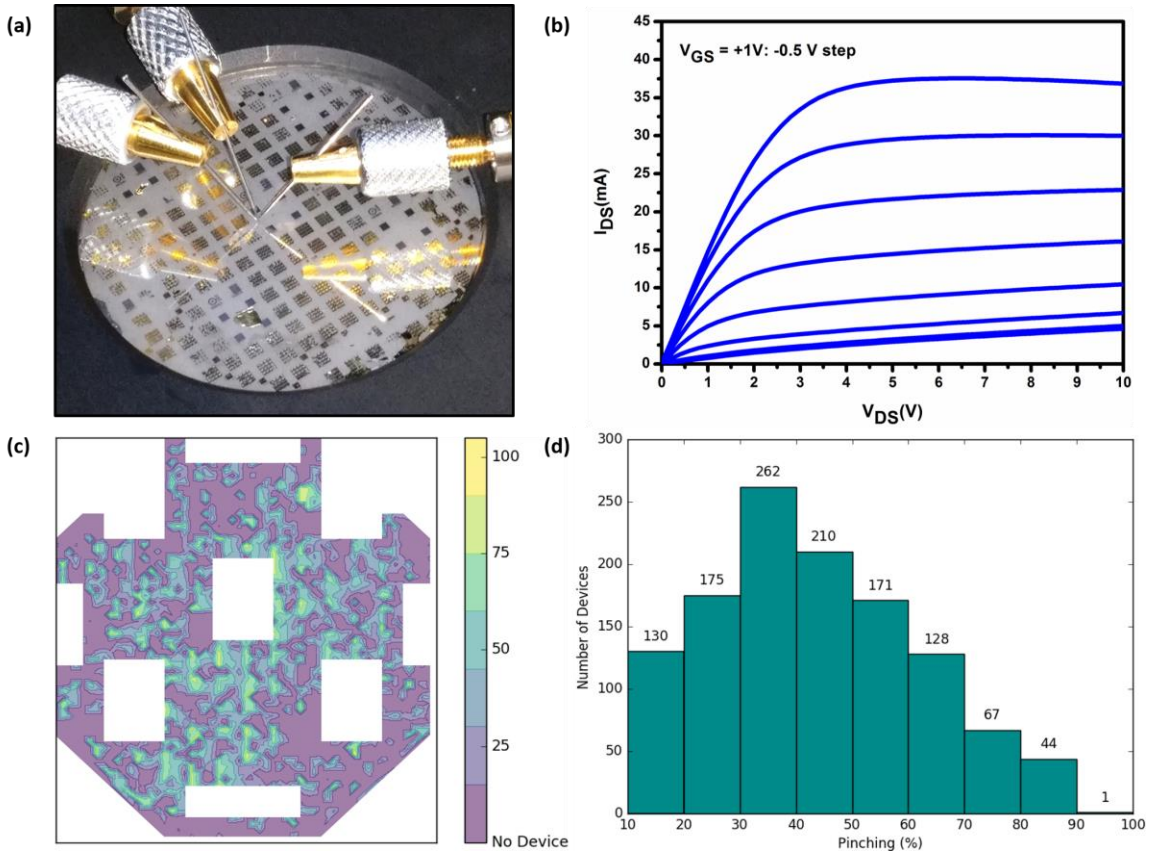

Figure 4-19 (a) Photo of the wafer-scale processed HEMT sensors, (b) I_{DS}-V_{DS} characteristic of an HEMT device with 2 µm gate length (c) Wafer mapping of the gate pinching, with white areas representing masked-off regions that include TLM patterns (d) Histogram of the pinching distribution across the wafer.

4.4.2 Sensor measurements: before and after transfer

HEMT gas sensors with greater than 80% gate pinching were tested under NO_2 gas for a concentration of 100ppm at 30 °C, both as-grown on the original sapphire substrate and after transfer to a tape with acrylic adhesive. The sapphire layer was removed by fixing supports to both the sapphire and active layer sides with a thermoplastic polymer, and applying pressure so that the Van der Waals bonds in the h-BN layer are broken. The active layers are then transferred to a flexible substrate; we have chosen to use a tape with acrylic adhesive for thermal insulation. The top support is removed by heating the thermoplastic at 60 °C and rinsing the residues with DI water.

Exposure to the gas leads to decreased drain-source current. From the transient response and recovery curves, we have calculated sensitivity as $S = [\,|\,I_0-I_{gas}\,|\,/I_0]*100$, where I_0 is the initial current under pure N_2 and I_{gas} is the steady state current after the test gas has been applied. This metric gives a normalized measure of the change in device current under gas exposure. We have also determined the response time τ defined by the time between 10% and 90% of the initial and final steady state values under gas exposure. The average sensitivity S was found to be 2.8 % ± 1.4 % with an average response time of 361 s ±140.8 s for around 20 tested devices. Figure 4-20 (a) presents one of the best response we obtained before the transfer, S and τ were calculated to be equal to 6.5 % and 385 s respectively. Working devices after the transfer to the new substrate have undergone the same testing procedure. The results indicate an average sensitivity S = 12 % ± 1.2 % with a response time ranging from 7s to 61 s. Figure 4-20 (b) shows result from the same device, used in figure 4-20 (a), after its transfer. This sensor presents a doubling in sensitivity, a six times lower response time and a faster recovery after gas exposure. We also note that a repeated measurement with 9 test cycles during more than three consecutive hours has been performed after the transfer exhibiting similar response and no significant drift, as shown in Figure 4-20 c.

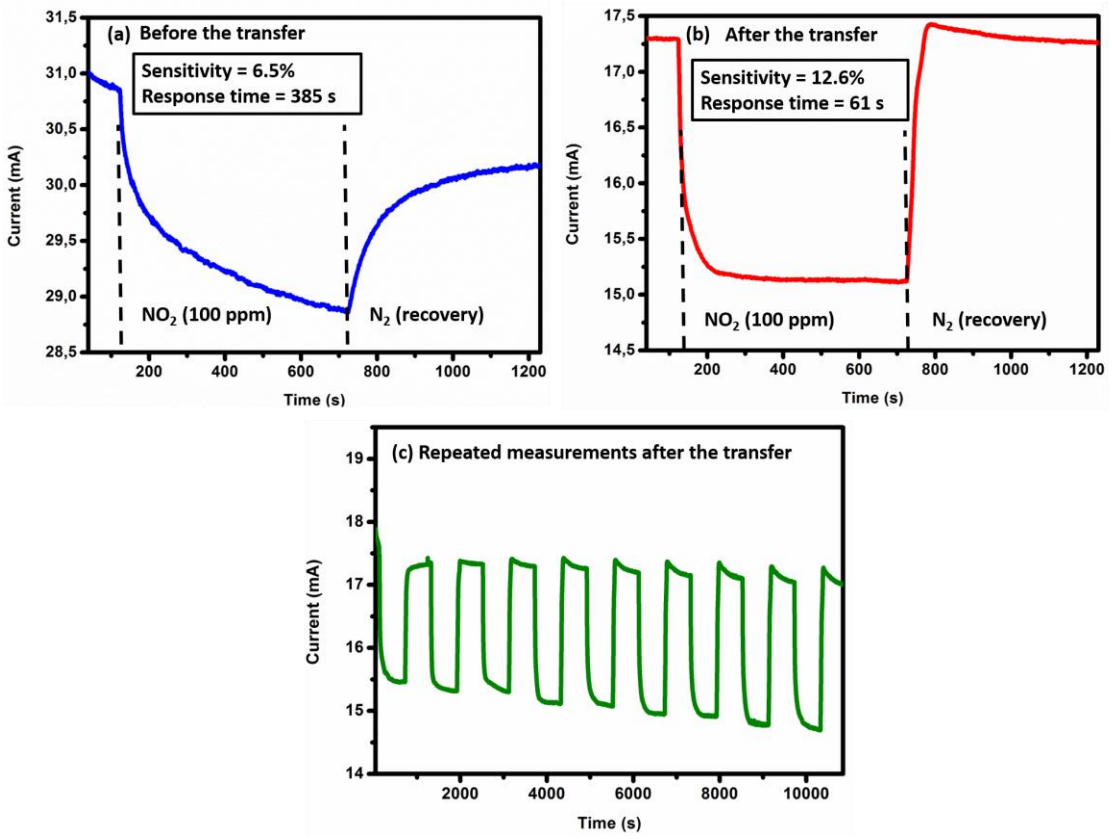

Figure 4-20 Response of n HEMT sensor, with a gate size of 2 μm × 200 μm, to NO_2 gas for a concentration of 100 ppm at 30°C. (a) Before the transfer, (b) after the transfer to the flexible template and (c) Repeated measure after the transfer showing the stability of the transferred device after 9 cycles.

The observed large enhancement in sensitivity and response time after transfer may be attributed to several root causes. Our choice of the final support is expected to enable the confinement of the heat generated by self-heating. As seen in Figure 4-21, thermal modeling results show that the tape with electrically conductive acrylic adhesive used in this study is predicted to yield a device operating temperature ranging between 105 °C and 128 °C. Thermal conductivities used in the simulation are 130 W/m.K for GaN, 25 W/m.K for Al0.14Ga0.86N, 20 W/m.K for Al0.25Ga0.75N, 19 W/m.K for Ti, 205 W/m.K for Al, 90 W/m.K for Ni, 314 W/m.K for Au, 72 W/m.K for Pt, and 385 W/m.K for copper. The temperature at the 25-micron thick copper film is 30 °C, the same as the chuck holder.

In addition, we have performed Raman spectroscopy measurements on the E_2 GaN line before and after transfer at different temperatures and with different input powers, based on the method reported in [96]. The Raman measurements show that pre-transfer self-heating results in a sensor temperature of 60 °C in the active region. After transfer, the sensor temperature was measured to be 120 °C. These results are consistent with thermal simulations presented in Figure 4-21. It also explains the drop in I_0 after transfer since device temperature is inversely related to the electron mobility in the 2DEG [97].

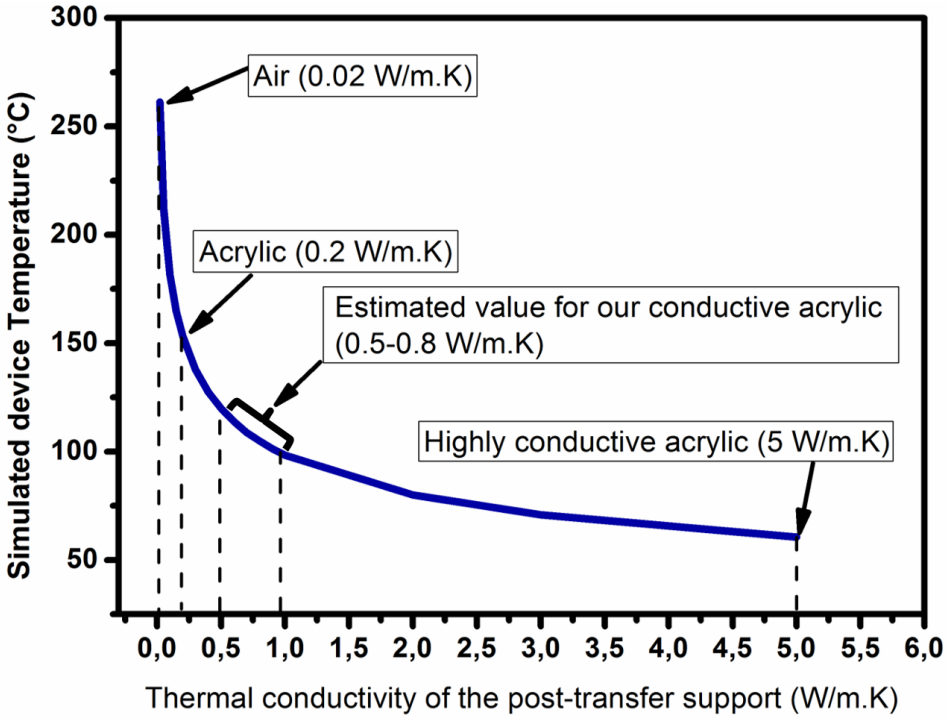

Figure 4-21 Thermal simulation of the operating device temperature Vs thermal conductivities of different post-transfer supports.

To verify whether this increase in device operating temperature is the primary reason behind the boosted performances, we have operated a pre-transfer sensor (on h-BN/sapphire) at 120 °C and compared the performance to the transferred sensor. The sensitivity and the response time of a pre-transfer device were measured as a function of temperature. The results show that the sensitivity has only increased by a factor of 1.06 when varying the stage temperature from 30 °C to 120 °C, and the response

time has decreased by a factor of 2.47. Because these factors are less than those resulting from the transfer (1.94 and 6.31, respectively), it suggests that other reasons in addition to thermal effects are behind the post-transfer performance enhancement.

The effects from strain changes in the semiconductor layers after the transfer may play a role and should be considered. Raman spectroscopy results, performed at room temperature both before and after transfer, show a relaxation of the GaN layer after the transfer. The E_2 peak of GaN has shifted towards less compressive strains, as presented in Figure 4-22 a, which agrees with the reported results in [98] and indicates an increase of the 2DEG carrier density. This is necessarily linked with an increase in the surface state charges to maintain the electrostatic neutrality[99], and can consequently contribute to the enhancement in sensitivity since the gas molecules are chemically absorbed to surface charges after dissociation on the Pt sensing layer[100].

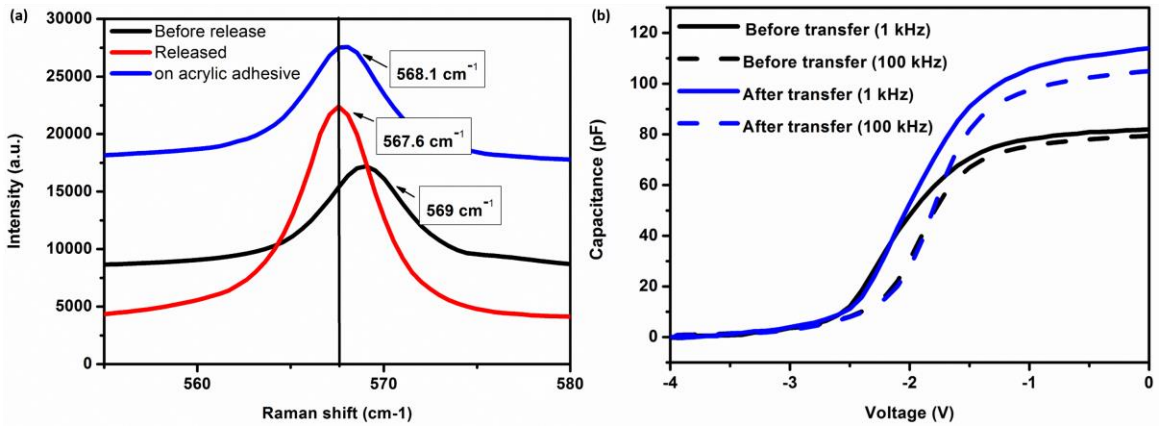

Figure 4-22 (a) Raman spectra at E2 peak of GaN on h-BN/sapphire (black), released from the sapphire (red) and transferred to an adhesive acrylic tape (red). (b) Capacitance-voltage measured at 1 kHz and 100 kHz on a device before and after its transfer. Both Raman and C-V results indicate an increase in the 2DEG density after the release and transfer to the acrylic adhesive tape.

To further confirm the increase in 2DEG carrier density, we have conducted C-V measurements at different frequencies between the gate and the source of a device before and after its transfer to the adhesive tape. From the C-V profiling in Figure 4-22 b, we observe a 39 % increase in maximum capacitance measured at 1 kHz after transfer which is directly related to the 2DEG carrier density at the AlGaN/GaN interface.

In this section, we have demonstrated wafer-scale fabrication of HEMT gas sensors grown on a 2-inch h-BN/sapphire template. The h-BN layer allowed the transfer of the devices to a flexible and heat insulating acrylic tape. Gas sensing measurements have been carried out before and after the transfer showing greatly improved performance on the flexible substrate.

These results confirm the feasibility of the h-BN enabled epitaxial lift off technique for wafer scale growth and fabrication of GaN-based devices and for their release and transfer to more suitable substrate with enhanced functionalities and performances. In the next chapter, we will focus on the application of this technique to heterogeneously integrate InGaN solar cells on foreign substrate.

CHAPTER 5. HETEROGENEOUS INTEGRATION OF THIN-FILM INGAN BASED SOLAR CELLS ON FOREIGN SUBSTRATES

In this section, we apply the h-BN enabled epitaxial liftoff technique to grow, fabricate and transfer InGaN-based solar cells from a 2-inch h-BN/sapphire template to a glass slab with a dielectric mirror (DM) reflecting only high energy photons, as illustrated in figure 5-1 a.

The choice of this final substrate enhances the performance of the InGaN-based solar cells thanks to the increased light absorption due to the reflected high energy photons. At the same time, the DM transmits longer wavelengths which allows the operation of a 4-terminal tandem device after bonding with Si or GaAs-based solar cells. Figure 5-1 b shows microscope images of two crack-free ~1mm^2 devices after their mechanical separation from the sapphire by means of a water-dissolvable tape. After liftoff, the devices are bonded on glass with a backside reflector using a polyurethane-based transparent resin, as shown in figure 5-1 c.

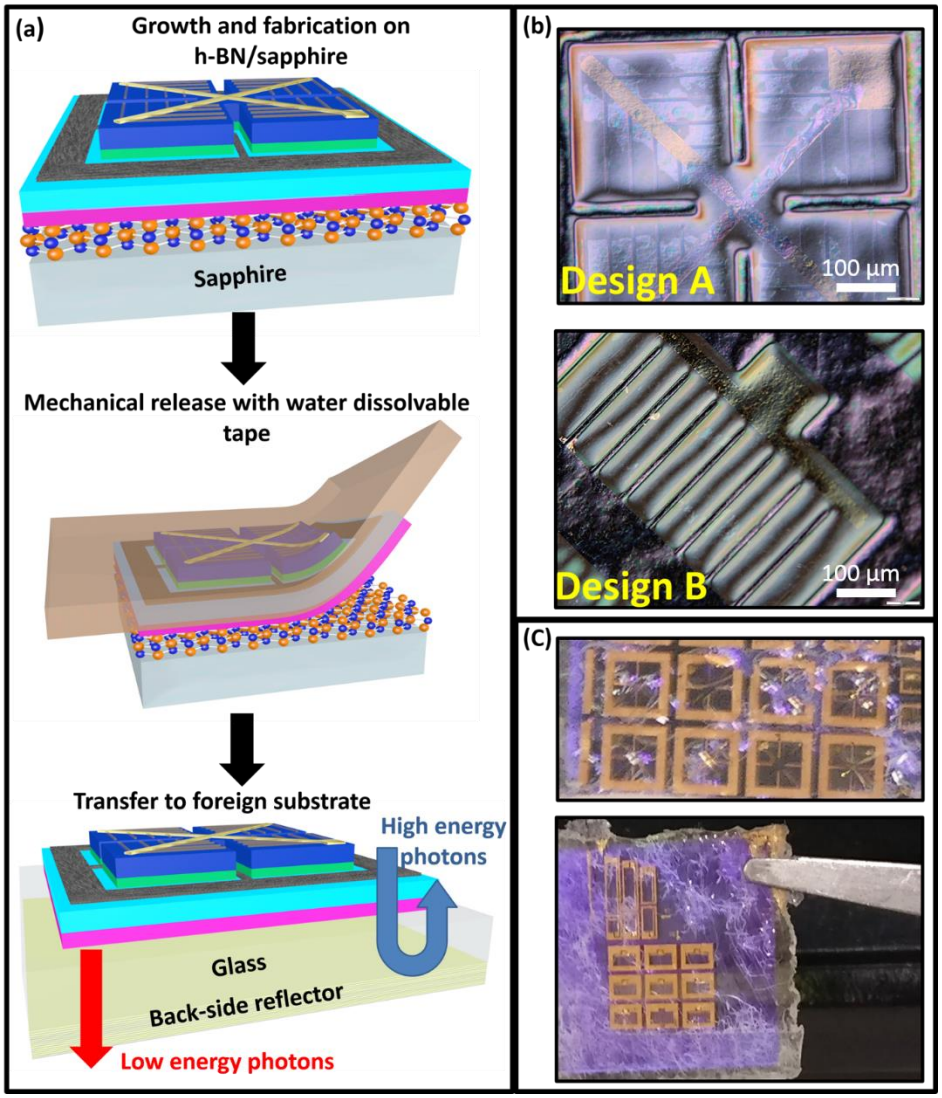

Figure 5-1 a) Schematics of fabrication steps for releasing InGaN-based solar cells from sapphire and transferring them onto foreign substrates. b) Optical microscopy images from the back side of ~1mm^2 solar cells with two different designs on a water dissolvable tape after release. c) Photographs of devices with different sizes and designs transferred to glass with a DM as a back-side reflector (the purple background is due to the reflected wavelength between 375-465 nm).

5.1 Materials growth by MOVPE

The growth was performed in an Aixtron MOVPE CCS 3x2'' system on a (0001) sapphire substrate. Triethylboron (TEB), Trimethylgallium/Triethylgallium (TMGa/TEG), Trimethylindium (TMIn) Trimethylaluminum (TMAl) and Ammonia (NH_3), were used as B, Ga, In, Al and N sources, respectively. Silane (SiH4) and Cp_2Mg was used as n-type and p-type doping sources. First, a h-BN layer (5 nm) was grown on the sapphire substrate at 1280°C. Then, an intermediate Si-doped AlGaN layer (300 nm) with an Al mole fraction of 14% was grown at 1100°C. The InGaN-based solar cell structure consists of a Si-doped GaN layer (0.5 µm), 5-periods of InGaN/GaN multi-quantum wells (MQWs), and a Mg-doped GaN layer (0.3 µm). The MQW structure consists of a 12 nm-thick GaN barrier layer and a 2.5 nm-thick InGaN quantum well layer. The growth of the GaN-based layers on the ultra-thin h-BN layer is governed by van der Waals epitaxy (vdWE)[101]. The high-resolution X-ray diffraction (HR-XRD) $2\theta - \omega$ scan around the (002) reflection of the grown structure is shown in figure 5-2 a. The scan clearly delineates the InGaN satellite peaks up to the fifth order as well as the peaks from the GaN and $Al_{0.14}GaN$ layers. Reciprocal space mapping shows a strained MQW structure (inset of figure 5-2 a). The In content extracted from X-ray simulation is around 18%. figure 5-2 b is the photoluminescence (PL) mapping performed at room temperature. Over the entire 2-inch wafer, the average emission wavelength is 475nm, which is in agreement with the HR-XRD In content, and the standard deviation of the peak wavelength is 0.8%. This series of structural and optical characterizations demonstrate the ability to grow epitaxial InGaN-based structures on a Van der Waal surface with good quality that can operate as photovoltaic devices.

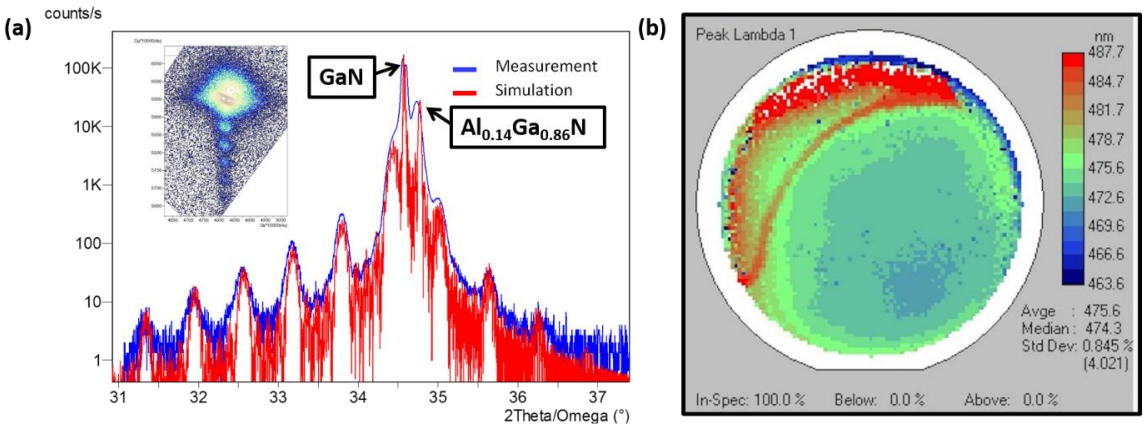

Figure 5-2 (a) HR-XRD 2θ – ω scan of the grown MQW structure (blue curve) with simulation (red curve); the inset shows the RSM. (b) Wavelength distribution of photoluminescence mapping performed at room temperature.

5.2 Wafer-scale devices fabrication

Several solar cells with different designs and sizes were fabricated using a 2-inch grown sample, as shown in figure 5-4 a. A standard photolithography-based process, shown in figure 5-3, has been applied while contact with liquids was limited and no ultrasonic cleaning was used. First, mesa etching isolation was achieved by inductively coupled plasma with BCl3/Cl2/Ar chemistry. Ti/Al/Ni/Au, Ni/Au and another Ti/Al/Ni/Au stack was used for the n-contact, the p-contact and the bus bars, respectively. All the metals layers have been deposited by thermal evaporation. N-contact annealing was carried out at 850 °C for 30 s under N_2; the p-contact was annealed at 600 °C for 60s under an O_2/N_2 atmosphere. Dark I-Vs were measured by an automated probe station and the photovoltaic results were obtained using an Oriel Sol3A solar simulator.

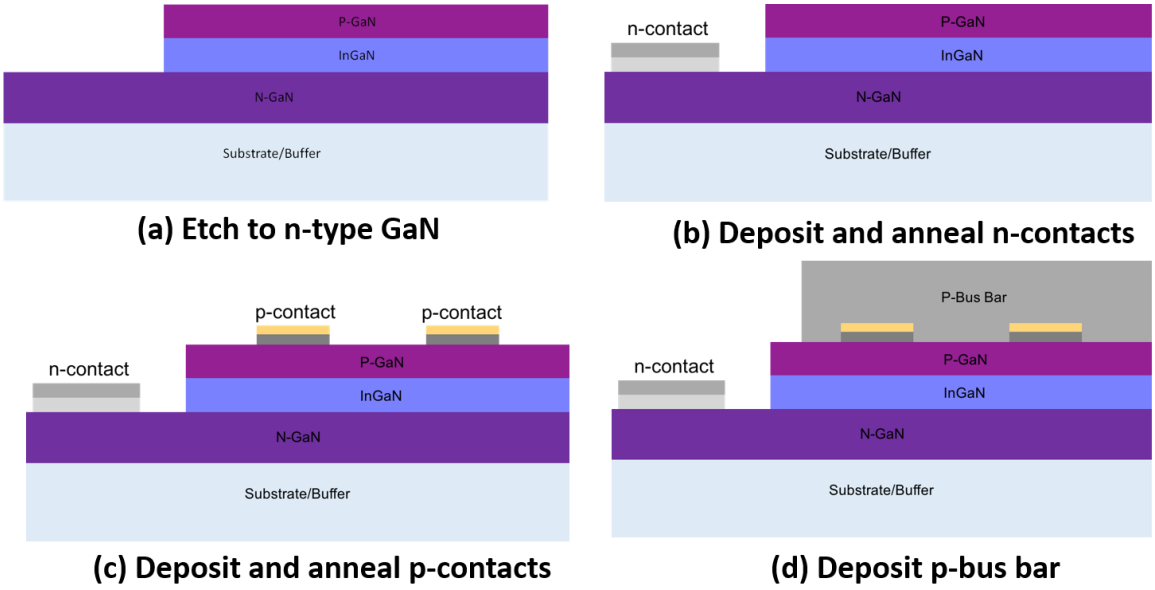

Figure 5-3 Process fabrication of the solar cells.

After fabrication, dark and illuminated I-V measurements were performed. The results for a set of devices having the same design and located at different positions on the wafer are presented in this paper. The dark I-V curves, shown in figure 5-4 c, demonstrate good process uniformity at the wafer scale. Figure 5-4 d exhibits the J–V curves under AM 1.5 condition. Extracted efficiency, fill factor, open circuit voltage and short circuit current density are respectively equal to 0.08%, 39.5, 1.17 V and 0.17 mA/cm^2. These performances are comparable with similar reported InGaN solar cell grown on sapphire [102].

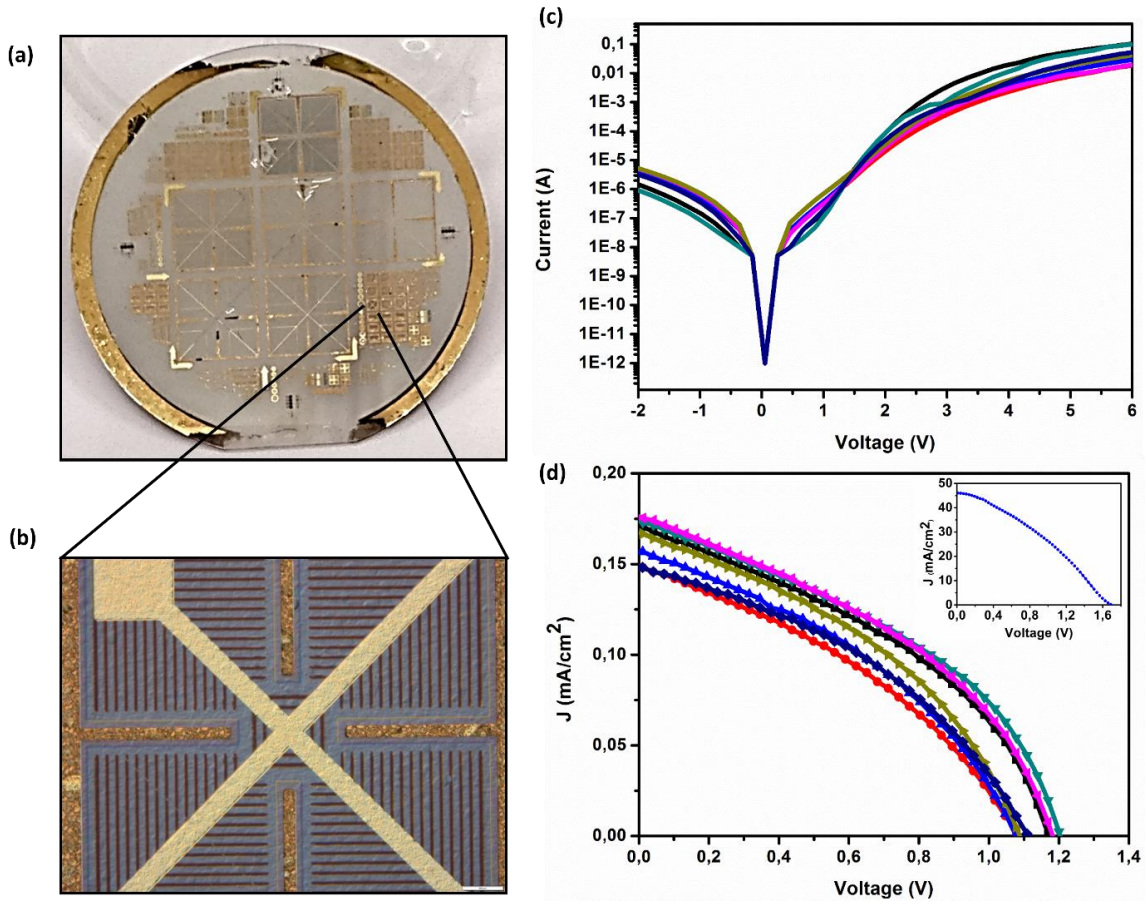

Figure 5-4 (a) Photograph of the fabricated solar cells on 2-inch h-BN/sapphire. (b) Optical microscopy image of a ~1mm^2 solar cell with design A. (c) Dark I-V curves of devices with design A in different locations on the wafer and their corresponding illuminated J-V curves under AM 1.5 condition in (d). Inset in (d) shows the illuminated J-V under a concentrated light source emitting at 440 nm.

To compare the experimental results to models, we have simulated the fabricated solar cell using commercially available SILVACO-Atlas software. Considering 35% of p-contact coverage, the simulation with AM 1.5 illumination condition results in an efficiency, a fill factor, an open circuit voltage and a short circuit current density equal to 0.14 %, 37.2, 2.28 V and 0.17mA/cm^2, respectively. The difference with the measured V_{oc} is mainly attributed to the barrier height from the p-contact. It is known that the formation of good ohmic contacts on p-doped GaN layers is difficult compared to on n-doped layers[103]. PV measurements using a lamp emitting at 440 nm with a power

density around 140 mW/cm^2 have been performed on several devices. They result in short circuit current densities J_{sc} of more than 40 mA/cm^2 and higher V_{oc} around 1.6 V as compared to the results under AM 1.5 condition as shown in the inset of Figure 5-4 d. These increased performances under high irradiance confirm the suitability of the InGaN solar cells for High Concentrated Photovoltaic (HCPV) applications.

5.3 Solar cells transfer on glass with back side reflector

After processing, the devices were easily transferred to a glass slab with a backside reflector by means of water dissolvable tape. The devices were bonded to the final substrate using an optically transparent polyurethane-based resin and the tape was removed in water without leaving residues. The transmittance of the resin is shown in the inset of Figure 5-6 (b).

The transfer method does not require any harsh chemicals or processing, and it is favorable for cost reduction since the growth substrate can be reused for future material depositions. During the transfer process, device structures remained completely intact and free from damage due to the gentle lift-off and transfer method. This is confirmed by the Transmission Electron Microscopy (TEM) image in Figure 5-5 (a) which shows the preservation of the MQW structure. Figure 5-5 (d) exhibits similar dark IV curves of a device (shown in the inset of Figure 5-5 (d)) before and after its release. This further confirms that no degradation has been induced from the transfer process.

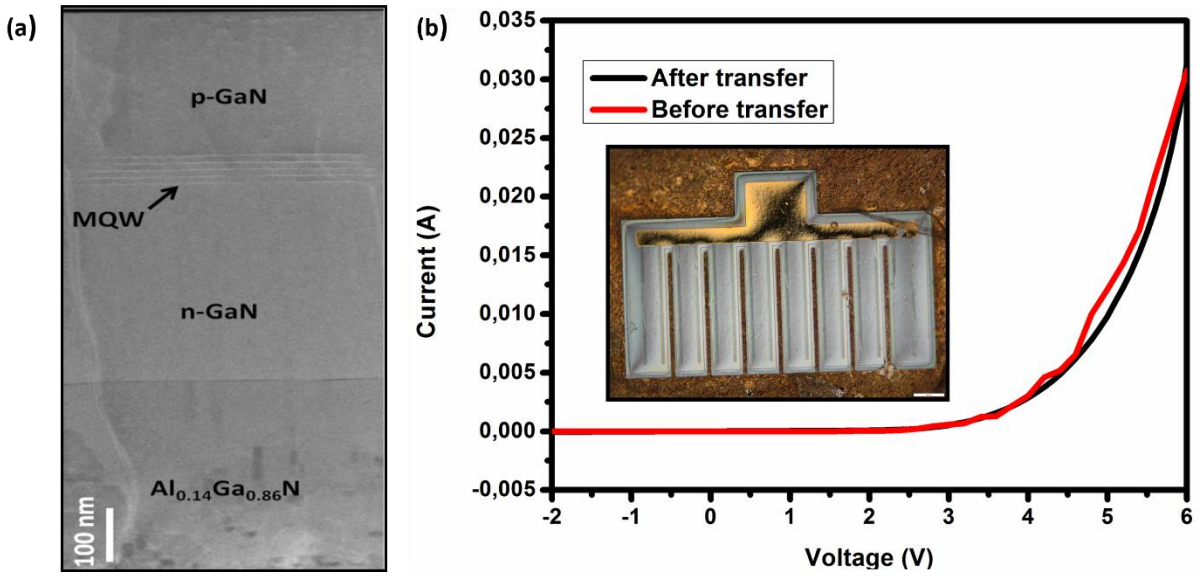

Figure 5-5 **(**a) High resolution TEM image of the grown structure after release from sapphire. (b) Dark IV curves of the same device before and after its transfer to a foreign substrate. Inset in (b) is an optical microscope image of a solar cell device after its transfer on the final substrate.

Two solar cell designs, shown in figure 5-1 b., were tested under AM 1.5 illumination condition before and after their transfer. In figure 5-6 c, we present the results for design A. In this case, the backside reflector is simply a 100-nm thick layer of Al that has around 90% reflectivity for the entire visible spectrum. This transfer resulted in a 20% increase in the J_{sc} since more light can be absorbed by the solar cell from the reflected photons.

For a 4-terminal tandem device with an InGaN-based solar cell on top, it is not possible to use an aluminum back reflector since it reflects the long-wavelength incident light. Hence, we designed a DM to selectively reflect wavelengths that can be absorbed by the InGaN cell and to transmit longer wavelengths. The DM was deposited on a glass substrate by Plasma-enhanced chemical vapor deposition (PECVD). It consists of 13 alternating layers of SiN (60 nm)/SiO2 (60 nm) and a final 140 nm SiN layer, as shown in figure 5-6 a. Fourier-transform infrared spectroscopy (FTIR) measurements on the deposited DM give reflectivity around 85% within the InGaN cell absorption spectrum and less than 20% for the higher wavelengths, as shown in figure 5-6 b.

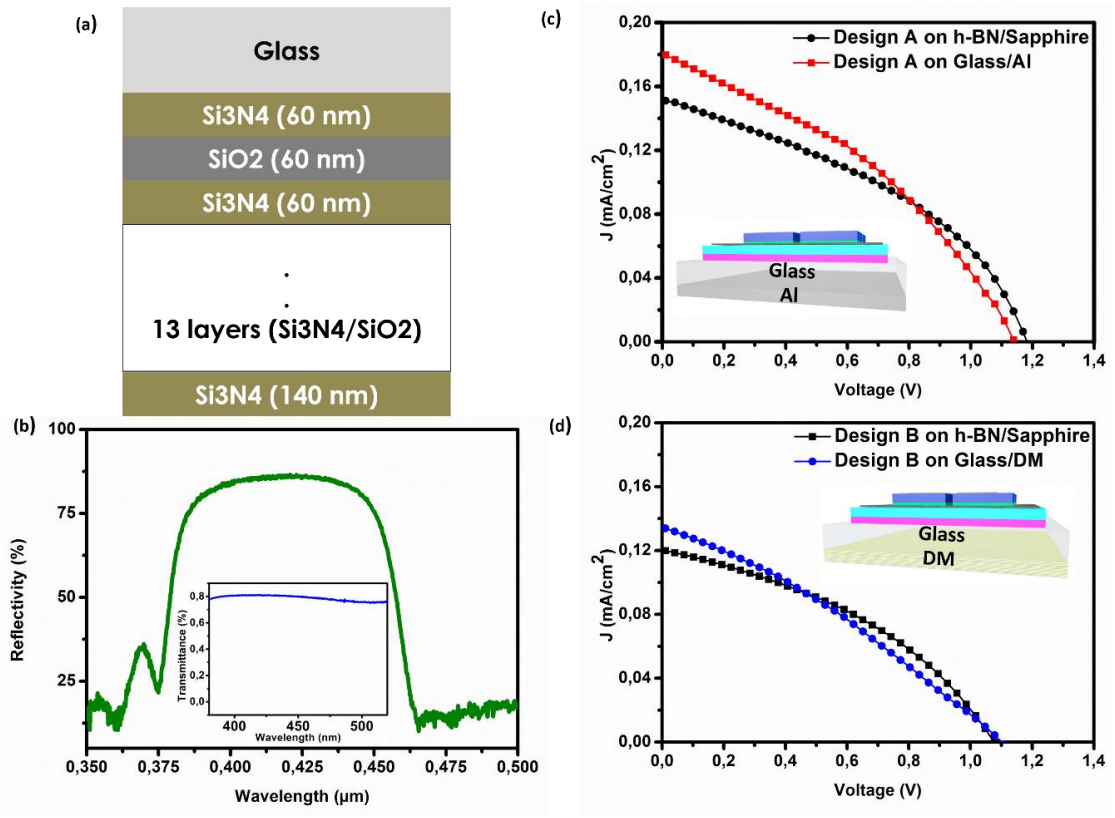

Figure 5-6 (a) Schematic of the deposited DM on glass. (b) FTIR measurements for the deposited DM on glass. (c) and (d) are J-V curves under AM 1.5 illumination condition of respectively a solar cell with design A before and after its transfer to a glass with Al back reflector and a solar cell with design B before and after its transfer to a glass with a dielectric mirror. Inset in (b) shows the transmittance of the polyurethane-based resin.

Solar cells with design B were transferred to a glass on which we deposited the designed DM. In this case, the reflected light has resulted in a J_{sc} increase by 12%, as shown in figure 5-6 d. The V_{oc} remained almost unchanged for both cases which indicates the preservation of the grown solar cell structure after the transfer process

In summary, this chapter presents an unprecedented growth and fabrication of InGaN solar cells using a 2-inch h-BN/sapphire wafer. The devices exhibit PV performances comparable to similar solar cells grown on sapphire. An easy, nontoxic and low-cost liftoff process was used to separate the devices from the growth wafer without cracks. After their release, thin-film solar cells are bonded on glass with a backside reflector. This transfer offers a new technological degree of freedom that allowed an increase in the J_{sc} up to 20% when placed on a back-side reflector. The results presented here provide viable routes to the development of advanced InGaN-based solar cells that can lead to a significant improvement in the efficiency and a cost reduction for both terrestrial and space photovoltaic applications.

CHAPTER 6. CONCLUSION AND PERSPECTIVES

6.1 Conclusion

The motivation behind this thesis work stems from the fact that a practical III-Nitride photovoltaic application consists of transfer to a foreign substrate with enhanced functionality and/or integration with mature group IV or III-V based solar cell technologies. This comes from the large lattice mismatch between InN and GaN that makes it experimentally difficult to grow good-quality, high In-composition InGaN films and currently impedes the realization of an all InGaN multi-junction solar cell. One interesting way to make hybrid solar cells is to grow and process the InGaN-based solar cell, release it from the growth wafer and bond it on top of the other cells. In this work, we have demonstrated an h-BN based epitaxial lift-off technique compatible with good quality III-N materials, with photovoltaic device fabrication and with subsequent bonding on a heterogeneous substrate.

We first optimized the growth conditions to obtain 2D layered h-BN with good homogeneity over a 2-inch sapphire wafer. The highly oriented lattice and hexagonal phase of the epitaxial layers were confirmed by X-ray diffraction, Raman spectroscopy, and cross-section scanning transmission electron microscopy. The surface of BN over a 2-inch wafer exhibits specific 2D material morphology features for different BN thicknesses, from an atomically flat surface to a honeycomb wrinkle network.

Secondly, we investigated the Van der Waal epitaxy of GaN-based materials on 2-inch h-BN/sapphire templates. InGaN based PIN structures and AlGaN/GaN heterostructures have been grown. Deep investigation of material quality is performed using structural, morphological and optical characterizations.

Thirdly, we have demonstrated the feasibility to fabricate devices grown on h-BN/sapphire at a wafer scale without spontaneous delamination that could be caused by the weak inter-layer bonding in the h-BN. HEMT-based gas sensors have been fabricated

and tested before and after their transfer on flexible substrate with enhanced sensing performance.

Finally, InGaN based solar cell structure has been grown on 2-inch h-BN substrate. Devices with various sizes and designs are processed and characterized on a full 2-inch wafer giving performances comparable to similar devices on sapphire. The subsequent crack-free transfer of the solar cells, enabled by Van der Waal bonded 2D layered h-BN, to a substrate with a backside reflector yields an increase in the short circuit current density of up to 20%. This demonstration of transferred InGaN-based solar cells on foreign substrates while increasing performance represents a major advance toward lightweight, low cost and high efficiency tandem photovoltaic applications.

6.2 Perspectives

- **Thicker InGaN based absorber**

To further increase the performance of our solar cells, we can use a semi-bulk InGaN absorber [58]. This approach is an effective method for achieving high efficiency InGaN PIN heterojunction solar cells. The semi-bulk absorber approach effectively helps to suppress the transition from two dimensional to three-dimensional growth that occurs during the growth of thick epitaxial InGaN layers.

Preliminary results have been already obtained for a semi-bulk InGaN based half PIN structure on 2-inch h-BN/sapphire substrate using $Al_{0.14}Ga_{0.86}N$ nucleation layer. Figure 6-1 shows the structural, morphological and optical characterizations of the grown structure.

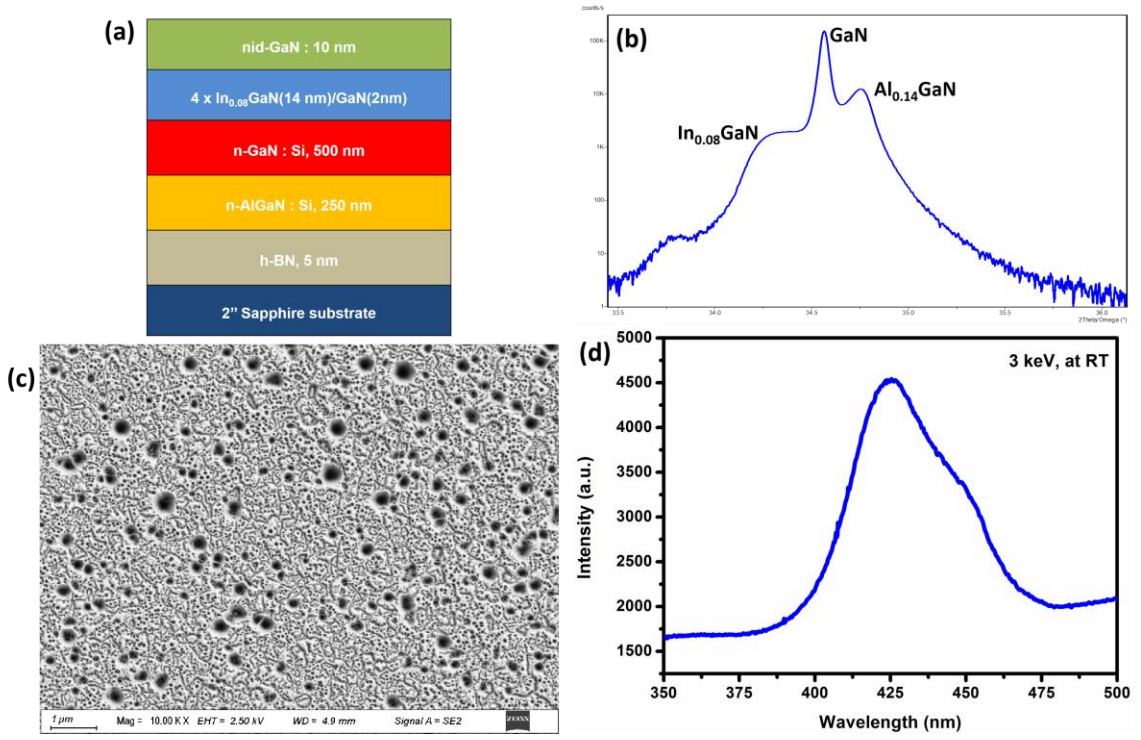

Figure 6-1 (a) Schematic illustration of the grown structure (b) HR-XRD 2θ – ω scan of the grown half PIN structure using semibulk InGaN, (c) SEM images of the grown structure surface and (d) CL spectrum recorded at room temperature under excitation of 3 keV.

- **PDMS-assisted transfer method**

The mechanical release and transfer of the grown structures may generate cracks and destroy the devices. This could be alleviated using an elastomeric stamp. Polydimethylsiloxane (PDMS) is a silicon-based polymer, easy to make and nontoxic. PDMS is made using pre-polymer and curing agent (Sylgard 184, Dow Corning Co., Midland, MI, USA). Thanks to its unique properties such as low stiffness, chemical stability, and conformal contact, PDMS can be used as a soft elastomeric stamp. It permits to transfer and print solid objects from one substrate to another and fabricate heterogeneous systems that integrates different devices [104]. The adhesion between the solid objects and the stamp is rate-sensitive (that is, kinetically controllable) owing to the viscoelastic behavior of the elastomer. A peeling with sufficiently high velocity (typically ~10 cm.s^{-1} or faster) leads to adhesion that is strong enough to

adhere preferentially the solid objects to the surface of the stamp. Then removing the stamp with sufficiently low peel velocity (~1mm.s^{-1} or slower) causes the objects to adhere preferentially to the device substrate and separate from the stamp. The process for PDMS assisted transfer is described in figure 6-2 [104].

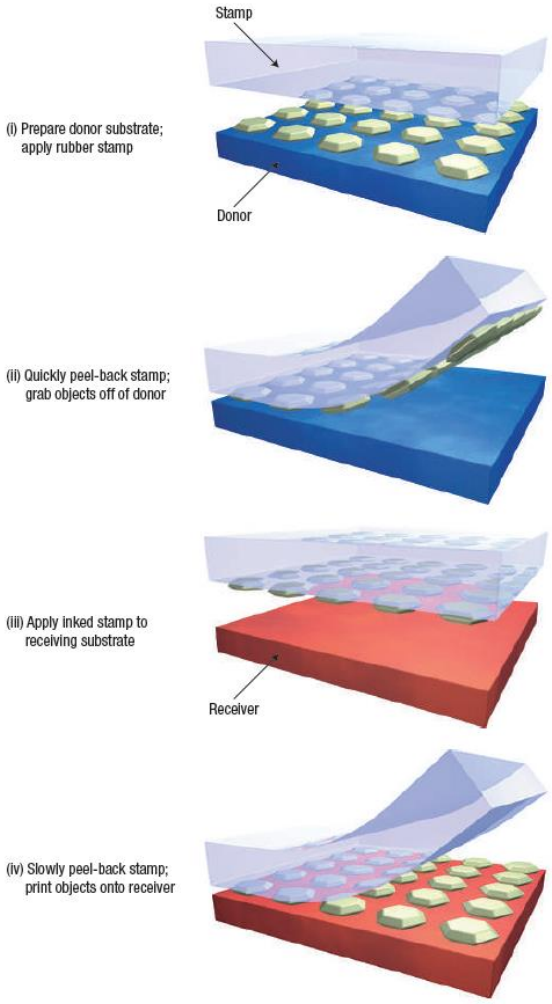

Figure 6-2 Schematic illustration of the generic process flow for transfer printing solid objects. The process begins with the preparation of an assemblage of microstructures on a donor substrate by solution casting, micromachining, self-assembly or other suitable means. (i) Laminating a stamp against a donor substrate and then quickly peeling it away (ii) pulls the microstructures from the donor substrate onto the stamp. Contacting the stamp to another substrate (receiving substrate (iii)) and then slowly peeling it away transfers the microstructures from the stamp to the receiver (iv). The peeling rate determines the strength of adhesion and, therefore, the direction of transfer [104].

- **Fabrication of a tandem device**

The transferred InGaN solar cells on the DM could be integrated on top of a Si cell to form a 4-terminal tandem device, as shown in figure 6-3. This could boost the current mature Si technology beyond the Shockley-Queisser limit. Simulations carried out for an InGaN/Si 4-terminal tandem device predicts an efficiency increase around 13% when adding a nitride solar cell with 20% In content[8].

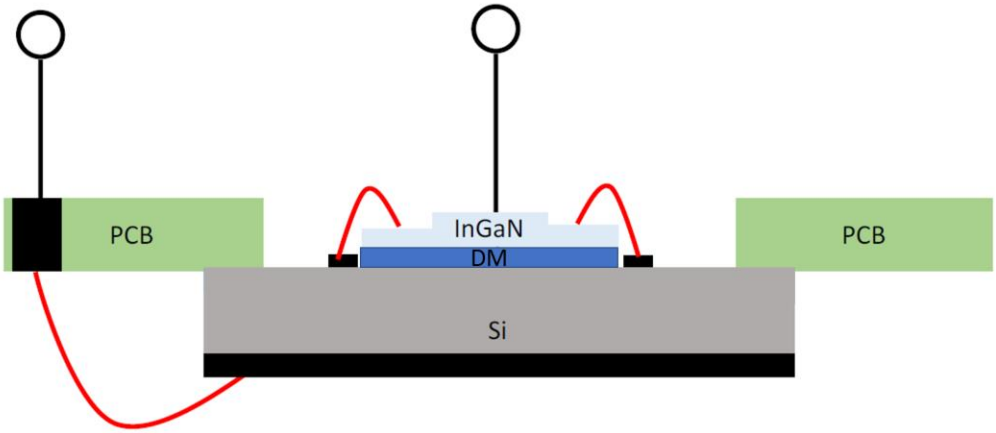

Figure 6-3 Design of a 4-terminal InGaN/Si tandem device

6.3 Publications

- **Peer-reviewed articles:**

Ayari Taha et al., "*Wafer-scale controlled exfoliation of metal organic vapor phase epitaxy grown InGaN/GaN multi quantum well structures using low tack two-dimensional layered h-BN*," Appl. Phys. Lett. **108, 171106**(2016).

Li Xin et al., "*Large area two-dimensional layered hexagonal boron nitride grown on sapphire by metal-organic vapor phase epitaxy*," Cryst. Growth Des. ***16, 3409–3415***(2016). (co-author).

Li Xin et al., "*Flexible metal-semiconductor-metal device prototype on wafer-scale thick boron nitride layers grown by MOVPE*," Scientific Reports, **7, 786** (2017). (co-author).

Ayari Taha et al., "Gas sensors boosted by two-dimensional h-BN enabled transfer on thin substrate foils: towards wearable and portable applications", Scientific Reports **7**, **15212**, (2017).

Ayari Taha et al., "Heterogeneous integration of thin-film InGaN-based solar cells on foreign substrates with enhanced performance", under revision.

- **Conferences:**

Oral presentation EMRS Spring 2017: *Investigation of GaN epitaxial growth on 2D layered h-BN by MOVPE at a wafer-scale.*

Oral presentation ICNS'12 Summer 2017: *Optimization of process fabrication of GaN-based heterostructure on h-BN for flexible gas sensors.*

Oral presentation EMRS Spring 2018: *Van der Waal Epitaxy investigation of GaN-based materials on 2D h-BN by MOVPE for high performance opto-electronic devices.*

Oral presentation ICMOVPE Summer 2018: *InGaN-based solar cells on 2D h-BN grown by MOVPE for hybrid tandem photovoltaic cells.*

- **Awards:**

  Young Scientist Award in recognition of an outstanding paper contributed to the 2018 E-MRS Spring meeting,

APPENDIX A: DEVICES FABRICATION

Apparatus

1) **Facilities:**

- 500 m^2 cleanroom at Institut Lafayette.

2) **Materials:**

- Relevant mask sets.
- Cleanroom supplies: tweezers, wipes, etc.

3) **Chemicals :**

- Cleaning: Acetone, Isopropanol, DI Water.
- Photoresist: Shipley® S1813, LOR 3b, SPR 220.
- Developer: Shipley® MF-319
- Buffered Oxide Etch (BOE)

4) **Tools:**

- **RTA:** As-One, ANNEALSYS
  - Temperature requirement: up to 860°C
  - Gases: N2, O2, air.

- **Mask Aligner:** EVG 6200
  - Should accommodate: Wafer size 2”
  - Minimum resolution: 0.5 - 1µm
  - Typical exposure wavelength – 350nm - 450nm, Broadband.

- **Etcher:** Inductively Coupled Plasma (ICP) Etcher, SPTS ICP process module
  - Should etch III-Nitrides (Cl2 diluted in Ar)
  - Should incorporate appropriate wafer size
  - Etch depths: 0.5 µm
  - Gases: Cl2, Ar, N2

- **E-Beam Evaporator:** Denton Vacuum Explorer
  - Metals: Ni, Au, Ti, Al

APPPENDIX B: ELECTRICAL CHARACTERIZATIONS

Hall effect measurements

Hall-effect experiments were used during this thesis to determine the carrier type, concentration, and mobility of grown epilayers. The standard procedure for the Hall effect experiments involves the following steps:

1. A 1 x 1 cm square specimen is cut from the sample.

2. Indium contacts are soldered to the four corners of the specimen. For this purpose, the soldering iron is heated at 400 C and is left in contact with indium droplets for 30 s.

3. The resistance between contacts is checked using a multi-meter.

4. The sample is positioned on the sample holder of the Hall-effect setup and the resistance of the contacts is measured again in this setup.

5. The sample holder is placed inside the magnet. Several (typically ten) measurements are taken and the average value is quoted as the result.

TLM measurements (Transfer Length Method)

Often the transfer length measurement method, or TLM method, is used to determine the specific contact resistance. In the TLM method ohmic contacts are formed on a semiconductor with varying distances between the two contacts. Typically, linear or circular contact designs are used as is shown in Figure B1.

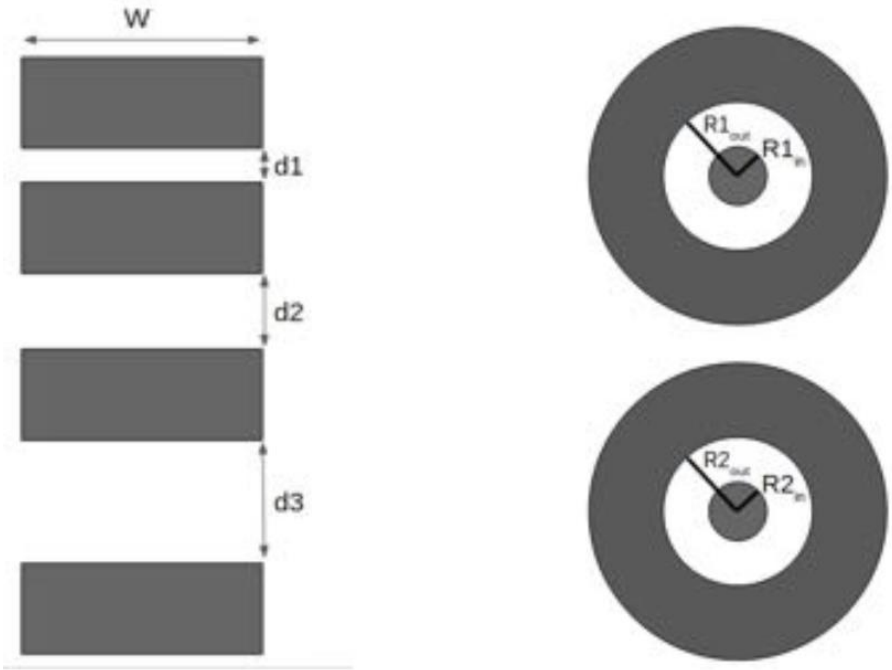

(a) Linear TLM (b) Circular TLM

Figure B1 Typical metal contact patterns for TLM measurements.

In this thesis work we have considered Linear TLMs. They are more simplistic to analyse. It is important that W >> di and that the material is either passivated or etched so that current is confined to flowing directly from one pad to the next. For simplicity we will confine our discussion to linear TLM patterns where these criteria are satisfied. Four–probe measurements are used on each of the pads to characterize the current–voltage characteristics for each of the gaps, d1, d2, etc. The resulting curves are fit to a linear model I = V/R + b. The parameter, b, should be very small (we are performing the measurements in the dark) but since we deal with physical data which can be noisy it is included because it increases the accuracy of the fit on the resistance and in a typical measurement it is 3–4 orders of magnitude less than the SMU (source measurement unit) range. This fitting is done by orthogonal distance regression and both the fit of the resistance in Ohms and the standard error of the fit are found for each of the gap distances di. In a typical measurement the resistance increases as the gap size increases and it is given by:

$$R(d) = \frac{Rsh}{W}\, d + 2\, \frac{Rsh\, Lt}{W} \tag{B.1}$$

And the specific contact resistance is given by:

$$\rho c = L_t^2\, R_{sh} \tag{B.2}$$

The results for R_{sh} (sheet resistance), L_t (transfer length: is the average distance a carrier travels under the contact before it is collected by the contact), and ρc are then obtained from the linear fit and the associated uncertainties from the standard errors of the fit.

REFERENCES

[1] K. Yoshikawa, H. Kawasaki, W. Yoshida, T. Irie, K. Konishi, K. Nakano, T. Uto, D. Adachi, M. Kanematsu, H. Uzu, and K. Yamamoto, "Silicon heterojunction solar cell with interdigitated back contacts for a photoconversion efficiency over 26%," *Nat. Energy*, vol. 2, no. 5, 2017.

[2] W. Shockley and H. J. Queisser, 'Detailed Balance Limit of Efficiency of p-n Junction Solar Cells,' J. Appl. Phys., vol. 32, p. 510, jun 1961.

[3] http://www.nrel.gov/ncpv/images/efficiencychart.jpg.

[4] 'Press release : NREL , CSEM Jointly Set New Efficiency Record with Dual-Junction Solar Cell,' Dec. 2015.

[5] 'Press release : Alta Devices Achieves 31.6% Solar Energy Efficiency Record , Changes the Fundamental Economics for Unmanned Aerial Vehicles,' Apr. 2016].

[6] I. Vurgaftman and J. R. Meyer, 'Band parameters for nitrogen-containing semiconductors,' vol. 94, no. 6, p. 3675, 2003.

[7] H. M., K. K., Y. T., S. Y., A. T., N. Y., T. N., and S. A., "Optical Properties of InxGa1—xN with Entire Alloy Composition on InN Buffer Layer Grown by RF-MBE," *Phys. status solidi*, vol. 234, no. 3, pp. 750–754, Dec. 2002.

[8] W. El-Huni, A. Migan, D. Alamarguy, and Z. Djebbour, “Modeling of InGaN/Si tandem cells: comparison between 2-contacts/4-contacts,” *EPJ Photovoltaics*, vol. 8, no. 85502, pp. 1–6, 2017.

[9] H. Search, C. Journals, A. Contact, M. Iopscience, and I. P. Address, “Large Free-Standing GaN Substrates by Hydride Vapor Phase Epitaxy and Laser-Induced Liftoff Large Free-Standing GaN Substrates by Hydride Vapor Phase Epitaxy and Laser-Induced Liftoff,” vol. 217, pp. 3–6, 1999.

[10] S. Mhedhbi, M. Lesecq, P. Altuntas, N. Defrance, Y. Cordier, B. Damilano, G. Tabares Jimenéz, A. Ebongue, and V. Hoel, “Recent improvements of flexible GaN-based HEMT technology,” *Phys. Status Solidi Appl. Mater. Sci.*, vol. 214, no. 4, pp. 4–8, 2017.

[11] K. Pantzas, D. J. Rogers, P. Bove, V. E. Sandana, F. H. Teherani, Y. El Gmili, M. Molinari, G. Patriarche, L. Largeau, O. Mauguin, S. Suresh, P. L. Voss, M. Razeghi, and A. Ougazzaden, “Chemical lift-off and direct wafer bonding of GaN/InGaN P-I-N structures grown on ZnO,” *J. Cryst. Growth*, 2015.

[12] W. S. Wong, T. Sands, and N. W. Cheung, “Damage-free separation of GaN thin films from sapphire substrates,” *Appl. Phys. Lett.*, vol. 72, no. 5, pp. 599–601, 1998.

[13] S. Tripathy, V. K. X. Lin, S. L. Teo, A. Dadgar, A. Diez, J. Bläsing, and A. Krost, “InGaN⁄GaN light emitting diodes on nanoscale silicon on insulator,” *Appl. Phys. Lett.*, vol. 91, no. 23, p. 231109, 2007.

[14] C.-Y. Cho, S.-J. Lee, S.-H. Hong, S.-C. Park, S.-E. Park, Y. Park, and S.-J. Park, “Growth and Separation of High Quality GaN Epilayer from Sapphire Substrate by Lateral Epitaxial Overgrowth and Wet Chemical Etching,” *Appl. Phys. Express*, vol. 4, no. 1, p. 12104, 2011.

[15] Y. Kobayashi, K. Kumakura, T. Akasaka, and T. Makimoto, “Layered boron nitride as a release layer for mechanical transfer of GaN-based devices,” *Nature*, vol. 484, no. 7393, pp. 223–227, Apr. 2012.

[16] T. Makimoto, K. Kumakura, Y. Kobayashi, T. Akasaka, and H. Yamamoto, "A vertical InGaN/GaN light-emitting diode fabricated on a flexible substrate by a mechanical transfer method using BN," *Appl. Phys. Express*, vol. 5, no. 7, 2012.

[17] T. Ayari, S. Sundaram, X. Li, Y. El Gmili, P. L. Voss, J. P. Salvestrini, and A. Ougazzaden, "Wafer-scale controlled exfoliation of metal organic vapor phase epitaxy grown InGaN/GaN multi quantum well structures using low-tack two-dimensional layered h-BN," *Appl. Phys. Lett.*, vol. 108, no. 17, 2016.

[18] T. Ayari, C. Bishop, M. B. Jordan, S. Sundaram, X. Li, S. Alam, Y. ElGmili, G. Patriarche, P. L. Voss, J. P. Salvestrini, and A. Ougazzaden, "Gas sensors boosted by two-dimensional h-BN enabled transfer on thin substrate foils: towards wearable and portable applications," *Sci. Rep.*, vol. 7, no. 1, p. 15212, 2017.

[19] H. Morkoc, *Handbook of Nitride Semiconductors and Devices*, WILEY-VCH. 2008.

[20] R. A. Ferreyra, C. Zhu, A. Teke, and H. Morkoç, "Group III Nitrides," in *Springer Handbook of Electronic and Photonic Materials*, S. Kasap and P. Capper, Eds. Cham: Springer International Publishing, 2017, p. 1.

[21] A. Costales, M. A. Blanco, Á. Martín Pendás, A. K. Kandalam, and R. Pandey, "Chemical Bonding in Group III Nitrides," *J. Am. Chem. Soc.*, vol. 124, no. 15, pp. 4116–4123, Apr. 2002.

[22] A. R. Denton and N. W. Ashcroft, "Vegard's law," *Phys. Rev. A*, vol. 43, no. 6, pp. 3161–3164, Mar. 1991.

[23] S. Azzi, A. Zaoui, and M. Ferhat, "On the importance of the band gap bowing in Boron-based III–V ternary alloys," *Solid State Commun.*, vol. 144, no. 5, pp. 245–248, 2007.

[24] A. Ougazzaden, S. Gautier, T. Moudakir, Z. Djebbour, Z. Lochner, S. Choi, H. J. Kim, J.-H. Ryou, R. D. Dupuis, and A. A. Sirenko, "Bandgap bowing in BGaN thin films," *Appl. Phys. Lett.*, vol. 93, no. 8, p. 83118, 2008.

[25] I. Vurgaftman, J. R. Meyer, and L. R. Ram-Mohan,‘Band parameters for III–V compound semiconductors and their alloys,’ J. Appl. Phys., vol. 89, no. 11, p. 5815, 2001.

[26] G. Orsal, Y. El Gmili, N. Fressengeas, J. Streque, R. Djerboub, T. Moudakir, S. Sundaram, A. Ougazzaden, and J. P. Salvestrini, “Bandgap energy bowing parameter of strained and relaxed InGaN layers,” *Opt. Mater. Express*, vol. 4, no. 5, pp. 1030–1041, 2014.

[27] F. Bernardini, V. Fiorentini, and D. Vanderbilt, “Spontaneous polarization and piezoelectric constants of III-V nitrides,” *Phys. Rev. B*, vol. 56, no. 16, pp. R10024--R10027, Oct. 1997.

[28] O. Ambacher, J. Smart, J. R. Shealy, N. G. Weimann, K. Chu, M. Murphy, W. J. Schaff, L. F. Eastman, R. Dimitrov, L. Wittmer, M. Stutzmann, W. Rieger, and J. Hilsenbeck, “Two-dimensional electron gases induced by spontaneous and piezoelectric polarization charges in N- and Ga-face AlGaN/GaN heterostructures,” *J. Appl. Phys.*, vol. 85, no. 6, pp. 3222–3233, 1999.

[29] B. F. and F. V., “Nonlinear Behavior of Spontaneous and Piezoelectric Polarization in III–V Nitride Alloys,” *Phys. status solidi*, vol. 190, no. 1, pp. 65–73, Mar. 2002.

[30] V. Fiorentini, F. Bernardini, and O. Ambacher, “Evidence for nonlinear macroscopic polarization in III–V nitride alloy heterostructures,” *Appl. Phys. Lett.*, vol. 80, no. 7, pp. 1204–1206, Feb. 2002.

[31] M. A. Moram and M. E. Vickers, “X-ray diffraction of III-nitrides,” *Reports Prog. Phys.*, vol. 72, no. 3, p. 36502, 2009.

[32] H. M. Manasevit, “SINGLE-CRYSTAL GALLIUM ARSENIDE ON INSULATING SUBSTRATES,” *Appl. Phys. Lett.*, vol. 12, no. 4, pp. 156–159, Feb. 1968.

[33] H. M. Manasevit, “The use of metalorganics in the preparation of semiconductor

materials: Growth on insulating substrates," *J. Cryst. Growth*, vol. 13–14, pp. 306–314, 1972.

[34] G. B. Stringfellow, "4 - Source Molecules," in *Organometallic Vapor-Phase Epitaxy (Second Edition)*, Second Edi., G. B. Stringfellow, Ed. San Diego: Academic Press, 1999, pp. 151–209.

[35] G. B. Stringfellow, "1 - Overview of the {OMVPE} Process," in *Organometallic Vapor-Phase Epitaxy (Second Edition)*, Second Edi., G. B. Stringfellow, Ed. San Diego: Academic Press, 1999, pp. 1–16.

[36] D. Gaskell, *Introduction to the Thermodynamics of Materials, Fifth Edition.* 2008.

[37] A. Mircea, A. Ougazzaden, and R. Mellet, "Very uniform epitaxy," *Prog. Cryst. Growth Charact.*, vol. 19, no. 1, pp. 39–49, 1989.

[38] B. Fultz and J. Howe, *Transmission Electron Microscopy and Diffractometry of Materials*. Berlin, Heidelberg: Springer Berlin Heidelberg, 2013.

[39] K. Pantzas, G. Patriarche, D. Troadec, S. Gautier, T. Moudakir, S. Suresh, L. Largeau, O. Mauguin, P. L. Voss, and A. Ougazzaden, "Nanometer-scale, quantitative composition mappings of InGaN layers from a combination of scanning transmission electron microscopy and energy dispersive x-ray spectroscopy," *Nanotechnology*, vol. 23, no. 45, p. 455707, 2012.

[40] G. Binnig, C. F. Quate, and C. Gerber, "Atomic Force Microscope," *Phys. Rev. Lett.*, vol. 56, no. 9, pp. 930–933, Mar. 1986.

[41] M. D., "Scanning electron microscopy 1928–1965," *Scanning*, vol. 17, no. 3, pp. 175–185, Jun. 2018.

[42] T. Coenen, B. J. M. Brenny, E. J. Vesseur, and A. Polman, "Cathodoluminescence microscopy: Optical imaging and spectroscopy with deep-subwavelength resolution," *MRS Bull.*, vol. 40, no. 4, pp. 359–365, 2015.

[43] J. Wu, W. Walukiewicz, K. M. Yu, W. Shan, J. W. Ager, E. E. Haller, H. Lu, W. J.

Schaff, W. K. Metzger, and S. Kurtz, “Superior radiation resistance of In1-xGaxN alloys: Full-solar-spectrum photovoltaic material system,” *J. Appl. Phys.*, vol. 94, no. 10, pp. 6477–6482, 2003.

[44] O. Jani, C. Honsberg, A. Asghar, D. Nicol, I. Ferguson, A. Doolittle, and S. Kurtz, “Characterization and analysis of InGaN photovoltaic devices,” in *Conference Record of the Thirty-first IEEE Photovoltaic Specialists Conference, 2005.*, 2005, pp. 37–42.

[45] C. J. Neufeld, N. G. Toledo, S. C. Cruz, M. Iza, S. P. DenBaars, and U. K. Mishra, “High quantum efficiency InGaN/GaN solar cells with 2.95 eV band gap,” *Appl. Phys. Lett.*, vol. 93, no. 14, p. 143502, 2008.

[46] E. Matioli, C. Neufeld, M. Iza, S. C. Cruz, A. A. Al-Heji, X. Chen, R. M. Farrell, S. Keller, S. DenBaars, U. Mishra, S. Nakamura, J. Speck, and C. Weisbuch, “High internal and external quantum efficiency InGaN/GaN solar cells,” *Appl. Phys. Lett.*, vol. 98, no. 2, p. 21102, 2011.

[47] Y. Kuwahara, T. Fujii, Y. Fujiyama, T. Sugiyama, M. Iwaya, T. Takeuchi, S. Kamiyama, I. Akasaki, and H. Amano, “Realization of Nitride-Based Solar Cell on Freestanding GaN Substrate,” *Appl. Phys. Express*, vol. 3, no. 11, p. 111001, 2010.

[48] R. Dahal, B. Pantha, J. Li, J. Y. Lin, and H. X. Jiang, “InGaN/GaN multiple quantum well solar cells with long operating wavelengths,” *Appl. Phys. Lett.*, vol. 94, no. 6, p. 63505, 2009.

[49] B. Wen Liou, “Design and fabrication of InxGa1 − xN/GaN solar cells with a multiple-quantum-well structure on SiCN/Si(111) substrates,” *Thin Solid Films*, vol. 520, pp. 1084–1090, 2011.

[50] N. G. Young, R. M. Farrell, Y. L. Hu, Y. Terao, M. Iza, S. Keller, S. P. DenBaars, S. Nakamura, and J. S. Speck, “High performance thin quantum barrier InGaN/GaN solar cells on sapphire and bulk (0001) GaN substrates,” *Appl. Phys. Lett.*, vol. 103, no. 17, p. 173903, 2013.

[51] N. G. Young, E. E. Perl, R. M. Farrell, M. Iza, S. Keller, J. E. Bowers, S. Nakamura, S. P. DenBaars, and J. S. Speck, "High-performance broadband optical coatings on InGaN/GaN solar cells for multijunction device integration," *Appl. Phys. Lett.*, vol. 104, no. 16, p. 163902, 2014.

[52] O. Jani, H. Yu, E. Trybus, B. Jampana, I. Ferguson, A. Doolittle, and C. Honsberg, "EFFECT OF PHASE SEPARATION ON PERFORMANCE OF III-V NITRIDE SOLAR CELLS," 2018.

[53] O. Jani, B. Jampana, M. Mehta, H. Yu, I. Ferguson, R. Opila, and C. Honsberg, "Optimization of GaN window layer for InGaN solar cells using polarization effect," in *2008 33rd IEEE Photovoltaic Specialists Conference*, 2008, pp. 1–4.

[54] B. R. Jampana, A. G. Melton, M. Jamil, N. N. Faleev, R. L. Opila, I. T. Ferguson, and C. B. Honsberg, "Design and Realization of Wide-Band-Gap (<formula formulatype='inline'><tex Notation='TeX'>sim</tex> </formula>2.67 eV) InGaN p-n Junction Solar Cell," *IEEE Electron Device Lett.*, vol. 31, no. 1, pp. 32–34, 2010.

[55] M. R. Islam, M. R. Kaysir, M. J. Islam, A. Hashimoto, and A. Yamamoto, "MOVPE Growth of InxGa1−xN (x ∼ 0.4) and Fabrication of Homo-junction Solar Cells," *J. Mater. Sci. Technol.*, vol. 29, no. 2, pp. 128–136, 2013.

[56] H. P. T. Nguyen, Y. L. Chang, I. Shih, and Z. Mi, "InN p-i-n Nanowire Solar Cells on Si," *IEEE J. Sel. Top. Quantum Electron.*, vol. 17, no. 4, pp. 1062–1069, 2011.

[57] B.-T. Tran, E.-Y. Chang, H.-D. Trinh, C.-T. Lee, K. C. Sahoo, K.-L. Lin, M.-C. Huang, H.-W. Yu, T.-T. Luong, C.-C. Chung, and C.-L. Nguyen, "Fabrication and characterization of n-In0.4Ga0.6N/p-Si solar cell," *Sol. Energy Mater. Sol. Cells*, vol. 102, pp. 208–211, 2012.

[58] K. Pantzas, Y. El Gmili, J. Dickerson, S. Gautier, L. Largeau, O. Mauguin, G. Patriarche, S. Suresh, T. Moudakir, C. Bishop, A. Ahaitouf, T. Rivera, C. Tanguy, P. L. Voss, and A. Ougazzaden, "Semibulk InGaN: A novel approach for thick, single phase, epitaxial InGaN layers grown by MOVPE," *J. Cryst. Growth*, vol.

370, pp. 57–62, 2013.

[59] M. Arif, “Investigation of new approaches for the realization of InGaN based solar cells.”, Thesis.

[60] S. Sundaram, R. Puybaret, Y. El Gmili, X. Li, P. L. Bonanno, K. Pantzas, G. Orsal, D. Troadec, Z.-H. Cai, G. Patriarche, P. L. Voss, J. P. Salvestrini, and A. Ougazzaden, “Nanoscale selective area growth of thick, dense, uniform, In-rich, InGaN nanostructure arrays on GaN/sapphire template,” *J. Appl. Phys.*, vol. 116, no. 16, p. 163105, Oct. 2014.

[61] R. Puybaret, G. Patriarche, M. B. Jordan, S. Sundaram, Y. El Gmili, J. P. Salvestrini, P. L. Voss, W. A. De Heer, C. Berger, and A. Ougazzaden, “Nanoselective area growth of GaN by metalorganic vapor phase epitaxy on 4H-SiC using epitaxial graphene as a mask,” *Appl. Phys. Lett.*, vol. 108, no. 10, 2016.

[62] B. W. H., “Bemerkungen über die Bildung von Verbindungen des Bors und Siliciums mit Stickstoff und gewissen Metallen,” *J. für Prakt. Chemie*, vol. 27, no. 1, pp. 422–430, Nov. 2004.

[63] Bernard Gil. Group III nitride semiconductors compounds, physics and applications. Oxford Science Publications, 1998.

[64] O. Fukunaga, “The equilibrium phase boundary between hexagonal and cubic boron nitride,” *Diam. Relat. Mater.*, vol. 9, no. 1, pp. 7–12, 2000.

[65] Ed. by M.E. Levinshtein et al., ‘Properties of advanced semiconductor materials GaN, AlN, InN, BN, SiC, SiGe,’ Scitech Book News, 2001.

[66] Y. Kobayashi, T. Akasaka, and T. Makimoto, “Hexagonal boron nitride grown by MOVPE,” *J. Cryst. Growth*, vol. 310, no. 23, pp. 5048–5052, 2008.

[67] A. Zunger, A. Katzir, and A. Halperin, “Optical properties of hexagonal boron nitride,” *Phys. Rev. B*, vol. 13, no. 12, pp. 5560–5573, Jun. 1976.

[68] http://www.ioffe.ru/SVA/NSM/Semicond/BN.

[69] I. Jo, M. T. Pettes, J. Kim, K. Watanabe, T. Taniguchi, Z. Yao, and L. Shi, "Thermal Conductivity and Phonon Transport in Suspended Few-Layer Hexagonal Boron Nitride," *Nano Lett.*, vol. 13, no. 2, pp. 550–554, Feb. 2013.

[70] R. S. Pease, "An X-ray study of boron nitride," *Acta Crystallogr.*, vol. 5, no. 3, pp. 356–361, 1952.

[71] A. Ismach, H. Chou, D. A. Ferrer, Y. Wu, S. McDonnell, H. C. Floresca, A. Covacevich, C. Pope, R. Piner, M. J. Kim, R. M. Wallace, L. Colombo, and R. S. Ruoff, "Toward the Controlled Synthesis of Hexagonal Boron Nitride Films," *ACS Nano*, vol. 6, no. 7, pp. 6378–6385, Jul. 2012.

[72] A. H. and M. C. and Z. C. and M. G. and H. Högberg, "Early stages of growth and crystal structure evolution of boron nitride thin films," *Jpn. J. Appl. Phys.*, vol. 55, no. 5S, p. 05FD06, 2016.

[73] T. Alam, B. Wang, R. Pulavarthy, M. A. Haque, C. Muratore, N. Glavin, A. K. Roy, and A. A. Voevodin, "Domain engineering of physical vapor deposited two-dimensional materials," *Appl. Phys. Lett.*, vol. 105, no. 21, p. 213110, Nov. 2014.

[74] Z. Zuo, Z. Xu, R. Zheng, A. Khanaki, J.-G. Zheng, and J. Liu, "In-situ epitaxial growth of graphene/h-BN van der Waals heterostructures by molecular beam epitaxy," *Sci. Rep.*, vol. 5, no. October, p. 14760, 2015.

[75] Y. Kobayashi and T. Akasaka, "Hexagonal BN epitaxial growth on (0001) sapphire substrate by MOVPE," *J. Cryst. Growth*, vol. 310, no. 23, pp. 5044–5047, Nov. 2008.

[76] Q. S. Paduano, M. Snure, J. Bondy, and T. W. C. Zens, "Self-terminating growth in hexagonal boron nitride by metal organic chemical vapor deposition," vol. 71004, no. 111, pp. 1–4, 2014.

[77] X. Li, S. Sundaram, Y. El Gmili, T. Ayari, R. Puybaret, G. Patriarche, P. L. Voss, J. P. Salvestrini, and A. Ougazzaden, "Large-Area Two-Dimensional Layered Hexagonal Boron Nitride Grown on Sapphire by Metalorganic Vapor Phase

Epitaxy," *Cryst. Growth Des.*, vol. 16, no. 6, pp. 3409–3415, 2016.

[78] L. Song, L. Ci, H. Lu, P. B. Sorokin, C. Jin, J. Ni, A. G. Kvashnin, D. G. Kvashnin, J. Lou, B. I. Yakobson, and P. M. Ajayan, "Large scale growth and characterization of atomic hexagonal boron nitride layers," *Nano Lett.*, vol. 10, no. 8, pp. 3209–3215, 2010.

[79] W. Paszkowicz, J. B. Pelka, M. Knapp, T. Szyszko, and S. Podsiadlo, "Lattice parameters and anisotropic thermal expansion of hexagonal boron nitride in the 10-297.5 K temperature range," *Appl. Phys. A Mater. Sci. Process.*, vol. 75, no. 3, pp. 431–435, 2002.

[80] C. K. Oliveira, E. F. A. Gomes, M. C. Prado, T. V. Alencar, R. Nascimento, L. M. Malard, R. J. C. Batista, A. B. de Oliveira, H. Chacham, A. M. de Paula, and B. R. A. Neves, "Crystal-oriented wrinkles with origami-type junctions in few-layer hexagonal boron nitride," *Nano Res.*, vol. 8, no. 5, pp. 1680–1699, 2015.

[81] K. Zhang and M. Arroyo, "Understanding and strain-engineering wrinkle networks in supported graphene through simulations," *J. Mech. Phys. Solids*, vol. 72, pp. 61–74, 2014.

[82] Z. Li, I. A. Kinloch, R. J. Young, K. S. Novoselov, G. Anagnostopoulos, J. Parthenios, C. Galiotis, K. Papagelis, C.-Y. Lu, and L. Britnell, "Deformation of wrinkled graphene.," *ACS Nano*, vol. 9, no. 4, pp. 3917–25, 2015.

[83] K. K. Kim, A. Hsu, X. Jia, S. M. Kim, Y. Shi, M. Hofmann, D. Nezich, J. F. Rodriguez-Nieva, M. Dresselhaus, T. Palacios, and J. Kong, "Synthesis of Monolayer Boron Nitride on Cu Foil Using Chemical Vapor Deposition," *Nano Lett.*, vol. 12, pp. 161–166, 2011.

[84] H. Cho, S. Park, D.-I. Won, S. O. Kang, S.-S. Pyo, D.-I. Kim, S. M. Kim, H. C. Kim, and M. J. Kim, "Growth kinetics of white graphene (h-BN) on a planarised Ni foil surface," *Sci. Rep.*, vol. 5, p. 11985, 2015.

[85] A. Koma, K. Sunouchi and T. Miyajima, Microelectron. Eng.,1984, 2, 129–136.

[86] A. Koma, “Van der Waals epitaxy-a new epitaxial growth method for a highly lattice-mismatched system,” *Thin Solid Films*, vol. 216, no. 1, pp. 72–76, 1992.

[87] A. Koma and K. Yoshimura, Surf. Sci., 1986, 174, 556–560.

[88] V. Kumaresan, “Novel substrates for growth of III-Nitride materials Novel substrates for growth of III-Nitride materials Présentée par Vishnuvarthan KUMARESAN,” 2017.

[89] M. Snure, G. Siegel, D. C. Look, and Q. Paduano, “GaN and AlGaN/GaN heterostructures grown on two dimensional BN templates,” *J. Cryst. Growth*, vol. 464, no. November 2016, pp. 168–174, 2017.

[90] Y. Kobayashi, K. Kumakura, T. Akasaka, and T. Makimoto, Nature 484, 223 (2012).

[91] G. Wang, D. Z. Yang, Z. Y. Zhang, M. S. Si, D. Xue, H. He, and R. Pandey, “Decoding the mechanism of the mechanical transfer of a GaN-based heterostructure via an h -BN release layer in a device configuration,” *Appl. Phys. Lett.*, vol. 105, no. 12, 2014.

[92] C. Bishop, Y. Halfaya, A. Soltani, S. Sundaram, X. Li, J. Streque, Y. El Gmili, P. L. Voss, J. P. Salvestrini, and A. Ougazzaden, “Experimental Study and Device Design of NO, NO_2, and NH_3 Gas Detection for a Wide Dynamic and Large Temperature Range Using Pt/AlGaN/GaN HEMT,” *IEEE Sens. J.*, vol. 16, no. 18, pp. 6828–6838, 2016.

[93] C. Bishop, “INNOVATIVE SENSORS USING NITRIDE SEMICONDUCTOR MATERIALS FOR THE DETECTION OF EXHAUST GASES AND WATER POLLUTANTS INNOVATIVE SENSORS USING NITRIDE SEMICONDUCTOR MATERIALS FOR THE DETECTION OF EXHAUST GASES AND WATER,” no. May, 2015.

[94] J. Song, W. Lu, J. S. Flynn, and G. R. Brandes, “Pt-AlGaN/GaN Schottky diodes operated at 800°C for hydrogen sensing,” *Appl. Phys. Lett.*, vol. 87, no. 13, p.

133501, Sep. 2005.

[95] Y. Halfaya, C. Bishop, A. Soltani, S. Sundaram, V. Aubry, P. L. Voss, J.-P. Salvestrini, and A. Ougazzaden, "Investigation of the Performance of HEMT-Based NO, NO(2) and NH(3) Exhaust Gas Sensors for Automotive Antipollution Systems," *Sensors (Basel).*, vol. 16, no. 3, p. 273, Mar. 2016.

[96] M. Nazari, B. Hancock, E. Piner, and M. Holtz, *Self-Heating in a GaN-Based Heterojunction Field-Effect Transistor Investigated by Ultraviolet and Visible Micro-Raman Spectroscopy*. 2015.

[97] R. Gaska, A. Osinsky, J. W. Yang, and M. S. Shur, "Self-heating in high-power AlGaN-GaN HFETs," *IEEE Electron Device Lett.*, vol. 19, no. 3, pp. 89–91, 1998.

[98] M. Hiroki, K. Kumakura, and H. Yamamoto, "Enhancement of performance of AlGaN/GaN high-electron-mobility transistors by transfer from sapphire to a copper plate," *Jpn. J. Appl. Phys.*, vol. 55, no. 5S, p. 05FH07, 2016.

[99] W. Xin-Hua, Z. Miao, L. Xin-Yu, P. Yan, Z. Ying-Kui, and K. Wei, *The physical process analysis of the capacitance—voltage characteristics of AlGaN/AlN/GaN high electron mobility transistors*, vol. 19. 2010.

[100] M. Ali, V. Cimalla, V. Lebedev, H. Romanus, V. Tilak, D. Merfeld, P. Sandvik, and O. Ambacher, "Pt/GaN Schottky diodes for hydrogen gas sensors," *Sensors Actuators B Chem.*, vol. 113, no. 2, pp. 797–804, 2006.

[101] M. I. B. Utama, Q. Zhang, J. Zhang, Y. Yuan, F. J. Belarre, J. Arbiol, and Q. Xiong, "Recent developments and future directions in the growth of nanostructures by van der Waals epitaxy.," *Nanoscale*, vol. 5, no. 9, pp. 3570–88, 2013.

[102] S. Valdueza-felip, A. Mukhtarova, Q. Pan, G. Altamura, L. Grenet, C. Durand, J. Eymery, E. Monroy, C. Bougerol, D. Peyrade, and F. Gonza, "Photovoltaic Response of InGaN / GaN Multiple-Quantum Well Solar Cells," *Jap. J. Appl. Phys.*, vol. 52, no. 1011, p. 08JH05, 2013.

[103] G. Greco, F. Iucolano, and F. Roccaforte, "Ohmic contacts to Gallium Nitride

materials," *Appl. Surf. Sci.*, vol. 383, pp. 324–345, 2016.

[104] M. A. Meitl, Z.-T. Zhu, V. Kumar, K. J. Lee, X. Feng, Y. Y. Huang, I. Adesida, R. G. Nuzzo, and J. A. Rogers, "Transfer printing by kinetic control of adhesion to an elastomeric stamp," *Nat. Mater.*, vol. 5, no. 1, pp. 33–38, 2006.

[105] K. Potje-Kamloth, "Semiconductor Junction Gas Sensors," *Chem. Rev.*, vol. 108, no. 2, pp. 367–399, Feb. 2008.

[106] S. J. Pearton, F. Ren, Y.-L. Wang, B. H. Chu, K. H. Chen, C. Y. Chang, W. Lim, J. Lin, and D. P. Norton, "Recent advances in wide bandgap semiconductor biological and gas sensors," *Prog. Mater. Sci.*, vol. 55, no. 1, pp. 1–59, 2010.